MSc Dissertation
Magnetic Properties in Diamond Induced by Proton Irradiation

Joyful Elma Mdhluli
(537099@students.wits.ac.za)
University of the Witwatersrand

Supervised by: Professor Elias Sideras-Haddad
University of the Witwatersrand

5 September 2017

Submitted to the Faculty of Science, Wits University

UNIVERSITY OF THE
WITWATERSRAND,
JOHANNESBURG

Declaration

I declare that this dissertation is my own work. It is being submitted in fulfilment of the requirements for the degree of Master of Science at the University of the Witwatersrand. It has not been submitted before for any degree or examination at any other university.

Joyful Elma Mdhluli.
Signed at: School of Physics
On the: 5^{th} of September 2017

Abstract

Ultra-pure type II-a diamond was irradiated with 2,2 MeV of protons with a fluence of $5.0 \times 10^{17} ions/cm^2$ at Universidad Autónoma de Madrid (UAM) using the 5 MV Tandem accelerator at the Centre for Microanalysis of Materials (CMAM). Magnetic measurements before and after irradiation were performed using the MPMS XL (5T) system that consists of the Superconducting Quantum Interference Device (SQUID) at the Consejo Superior de Investigaciones Cientficas (CSIC). The sample was further characterised using low temperature magnetic field microscopy (MFM) and Raman Spectroscopy.

The magnetization curves of the pristine (un-irradiated) sample exhibited an almost perfect diamagnetic signal which was independent of temperature. The diamagnetic signal obtained was 4.75×10^7 emu/g and was in agreement with that found in literature [1]. A very weak magnetic contribution was observed at 4.2 K though not at room temperature in the pre-irradiation measurements. The magnetization curves at 300 K and 4.2 K after irradiation and the thermal cycle at 2 kOe exhibited a similar diamagnetic behaviour to that of the pristine sample with a small and positive magnetic contribution appearing above the previous diamagnetic background. The main outcome of the irradiation seemed to be a paramagnetic contribution but there were additional superparamagnetic and ferromagnetic-like contributions which were also observed.

Raman spectra indicate graphitization on the irradiated area. An apparent blueshit was observed in the main diamond peak that was relative to 1332 cm^{-1}. The irradiated region that was not graphitized showed a little disorder within the structure of diamond as expected on an area that was heavily irradiated by protons. The damage was tens of microns into the sample. The graphitized region showed the G-peak at around 1600 cm^{-1} of the damaged diamond that is beyond the graphitization limit. The irradiated region showed a mixture of the $sp3$ and $sp2$ orbitals that are related to the peak at 1330 cm^{-1} of diamond and the 1580 cm^{-1} peak related to the G-band of graphite. The $sp2$ orbitals corresponded to the micro-polycrystalline graphite that is often seen in irradiated diamond. It has been previously observed that the defects have a tendency of clustering into graphitic islands and swell after high dose implantations.

Magnetic measurements show a decrease in the diamagnetic signal of the sample showing that the irradiation has affected the magnetic signal of the sample. A magnetic signal was observed in the MFM image with a negative contrast, this was observed by the darker regions relative to the pure diamond corresponding to the graphitic/graphitized region in the topography image. The negative contrast was not completely clear in the MFM image but it can be observed that there is a change in contrast between the irradiated and un-irradiated region.
From the SQUID analyses, Raman measurements and MFM analysis, we can safely conclude that the irradiation resulted in the mixture of $sp2$ and $sp3$ orbitals that graphitized the irradiated surface. As it was concluded from the Raman analyses, any magnetic signal measured over the graphitized irradiated region is attributed to the ion induced modification of the diamond structure.

Acknowledgements

I would like to extend my greatest gratitude to my supervisor Professor Elias Sideras-Haddad. Thank you Prof for granting me the opportunity to work with you. During the course of my MSc, I have gained an enormous amount of knowledge and this would not have been possible if you did not believe in me. You having me as your student has given me so many opportunities to learn and expand my expertise. Words will not describe how grateful I am to have had you as my supervisor throughout my MSc.

I would also like to extend my gratitude to our collaborators from C-MAM and CSIC in Madrid. A special thank you to Miguel Ramos, Carmen Munuera, Mar Garcia Hernadez and Maria Ysna for their contribution in the experimental aspect and analysis of the data. Your valuable input and comments helped put things into perspective. I would also like to thank the staff that was involved from CMAM during the experimental procedure.

I would also like to extend my deepest gratitude to Robyn Evans and Chan*é* Moodley. Your support throughout the years means a lot to me. Thank you both for reading my dissertation and giving me comments, it is very satisfying knowing that atleast two people have read my work. Thank you so much for being wonderful friends.

A special thank you to my mother, Ellen Mdhluli, for all the support you have given me all these years. You have been an inspiration to me and this has allowed me to dream big. Thank you for supporting my dreams and allowing me to be my own person. All that I am and aspire to be is all because of you and for that I am eternally grateful. A big thank you to my mother's sisters, Yvonne Mthembi and Sbongile Mathumba, your love and support has kept me going throughout. Thank you for encouraging me to fulfil my dreams even if they make no sense to you.

Thank you to all my friends and family, for keeping up with my madness and your support. I would like to name you all but it would be a very long list and I am afraid I might forget someone. So thank you to each and everyone of you for encouraging me when I needed encouragement and being

there when I needed someone around.

Lastly I would like to thank Veli Mathumba for all the support you have shown. It is unfortunate that you will never be able to read this but I am eternally grateful for the love and support you showed me when you were still with us. I therefore dedicate this dissertation to you.

Contents

List of Figures

Chapter 1

Introduction

1.1 Research Background

Magnetism in carbon has been widely studied since the early ages, the first paper solving the mystery of ferromagnetism was published in 1928 [11] by Heisenberg after his appointment at the University of Liepzig. Heisenberg's explanation of ferromagnetism paved way for various studies of magnetism in carbon structures. Theoretical [12] and experimental [13] results have been reported in literature since then. In 1968, N. Mutaga reported possible ferromagnetic states in hypothetical hydrocarbons. In his paper he stated that "hydrocarbons with conjugate π-electron systems may show ferromagnetic spin alignment due to the topology of the molecular orbitals" [12]. S. Mizogami et al. reported ferromagnetic pyrolytic carbon in 1989. This ferromagnetism was achieved by using adamantane as a starting material and the chemical vapour deposition (CVD) method under low temperature growth. In this paper they reported ferromagnetism at temperature T = 10 K; a saturation magnetization of $M_s = 0.5 emu/g$, a remanent magnetization of $M_r = 0.35 emu/g$, a coercive field of $H_c = 600 Oe$ and Curie temperature of $T_c = 400 K$ were all measured [13]. After that year, macroscopic magnetic ordering phenomena in organic materials such as $p-NPNN(C_{13}H_{16}N_3O_4)$, $[TDAE]^+C_{60}^-(CN_2(CH_3)_2)_2^+C_{60}^-$, amorphous-like carbon and fullerenes were also reported after performing various experiments [14] [15] [16] [17].

In November 2003, a group in the University of Leizig reported magnetic ordering in graphite induced by proton irradiation[18]. Highly ordered pyrolytic graphite (HOPG) samples were irradiated with protons of energy $2.25 MeV$, the irradiation triggered ferro- and ferrimagnetism [18]. The origin of magnetic ordering in carbon-based structures was studied by A.A. Ovchinnikov and V. N. Spector [19]. They found that the magnetic ordering is related to carbon atoms mixing of sp^2 and sp^3 bonds. These mixtures were predicted to reach a magnetization higher than that in pure

iron (Fe). K. Murata et al, amongst others, created a range of theories that include the assumption that hydrogen only plays a role in the formation of amorphous-carbon structure while others showed that hydrogenated graphite only displays spontaneous magnetization that comes from different numbers of mono- and dehydrogenated carbon atoms. Other theoretical predictions made were that spontaneous magnetization also appears in the case of mono-hydrogenated zigzag edges where the distance between them is large or they are non-parallel [17] [20] [21].

In their paper, the Liepzig group reported measurements performed on the samples before and after irradiation[18]. A ferromagnetic signal of the HOPG was shadowed by the diamagnetic signal coming from the silicon substrate for fields that were applied parallel to the graphene layers due to the small mass of the sample. Rutherford backscattering spectroscopy (RBS) and particle induced x-ray emission (PIXE) spectra were recorded to ensure that the sample was uncontaminated throughout the study. For comparison between the irradiated and non-irradiated samples, the atomic force microscope (AFM) and the magnetic force microscope (MFM) were used to characterize the different areas. Magnetization measurements were performed using the superconducting quantum interference device (SQUID) magnetometer. Monte Carlo simulations were performed using the Stopping Range of Ions in Matter (SRIM) 2013 to estimate the defect that would be caused by a 2.25 MeV proton beam. From their MFM and SQUID measurements, they observed that the proton irradiated spots on the HOPG samples showed that it is possible to create ferromagnetic active areas of $1\mu m^2$ with sharp borders of a magnetic force gradient. These areas appeared mostly at low proton dosages. This implies that it is possible to create micro-structures of arbitrary shape from a proton beam scanning system. They concluded from their measurements and results that magnetic ordering appears after proton irradiation in graphite and they also showed that it is stable in room temperature [18].

A few years ago, a group from the School of Physics in the University of the Witwatersrand decided to repeat the same experiment performed by the Liepzig group following the logic that if magnetic ordering can be induced in HOPG, then the same can be done in diamond since they are both carbon allotropes. The Wits group investigated the magnetic properties of ultra-pure type IIa diamond following irradiation with proton beams of approximately 2 MeV energy. Results from SQUID magnetometry indicated the formation of Curie type paramagnetism according to the Curie law. A strong correlation between vacancy production, proton fluence and the paramagnetic factor was observed. However, no evidence of long range magnetic ordering was observed at temperatures down to 4.2 K, even after annealing at temperatures of up to 1100 K. When a proton micro-beam

($10\mu m$) was used, there was evidence of magnetic ordering in type IIb single crystal synthetic diamond and therefore micro-beam irradiations were required in order to investigate this in more detail.

AFM and MFM measurements revealed magnetic signatures corresponding to the micro-irradiated micro-regions. From the SQUID, a magnetic hysteresis loop was observed at 2 K, these results led to the registration of a patent with Wits Enterprise. Similar studies performed in Nitrogen rich type Ib diamonds showed a superparamagnetic-like signal at 300 K. After the proton irradiation, a Curie-like paramagnetic curve was observed for thermal cycles at an applied magnetic field of 2 kOe which exhibits a transition at temperatures around 50-55 K. The hysteric behaviour below these temperatures has been interpreted as a transition from diamond to amorphous or glassy carbon which occurs as a direct result of the irradiation [22] [23].
To continue on this work, we tried to induce magnetic ordering in ultrapure type IIa diamond through proton irradiation using a micro-beam line with proton energy 2.2 MeV. The irradiated areas were characterised using SQUID magnetometry and low temperature MFM.

1.2 Dissertation Outline

This dissertation consists of 6 chapters with each chapter building up to the main goal of the current study. Chapter 1 covers the research background that lead to the study. In chapter 2, the material under, diamond, study is characterized starting with a review about its various properties which will be followed by a discussion about the material is synthesized and how it behaves under ion implantation.

Chapter 3 focuses on the various types of magnetism and how they behave in carbon structures. Diamagnetism is the most common type of magnetism found in carbon structures and will therefore be discussed first. Paramagnetism, ferromagnetism and finally superparamagnetism will be discussed thereafter.

A number of instruments were used in order to fulfil the aims and objectives of the study. A detailed discussion about each of these instruments will be included in Chapter 4. The Superconducting Quantum Interference Device (SQUID) was used for measuring very sensitive magnetic signals, the 5 MV tandem accelerator was used for the micro-irradiation of the sample, the magnetic field microscope (MFM) was used to characterise the irradiated area of the sample and Monte Carlo simulations were performed to estimate the radiation damage caused by vacancy production.

Chapter 5 focuses on the results and analysis of the data obtained. The data from the various techniques used is discussed in subsections. Chapter 6 concludes the dissertation where final comments and conclusions from the study are discussed.

Chapter 2

Diamond

2.1 Introduction

The diamond structure is made up of a carbon atom bonded to four other carbon atoms, with bonds of equal strength. A carbon atom in ground state consists of six electrons with the electron configuration $1s^2 2s^2 2p^2$. Unfortunately, the electron configuration does not take into account the tetrahedral symmetry of the diamond structure. In order to accommodate the tetrahedral symmetry, the carbon structure needs to be altered. The structure is altered to a state where the carbon atom has four valence electrons instead of two with each electron in a separate orbital and with uncoupled spin from the other electrons. When one electron in the L shell of the ground-state atom is moved from the $2s$ orbital to the $2p$ orbital, new orbitals are formed known as hybrids. These hybrids are a result of the combination between $2s$ and $2p$ orbitals.

Hybrid atomic orbitals are formed to alter the carbon structure that accounts for the tetrahedral symmetry of the diamond structure. The hybrid atomic atoms are denoted as $2p^3$ orbitals since they are a combination of one s orbital and three p orbitals. The process where hybrid orbitals are formed is known as hybridization and is better illustrated in Figure 2.1.

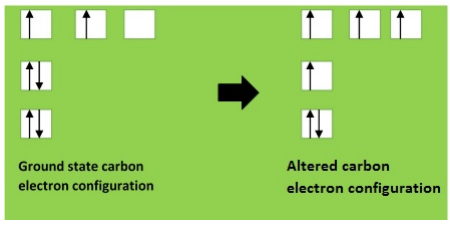

Figure 2.1: Electron configuration of ground state and altered carbon atom.

The atomic structure of diamond has tetrahedral symmetry and a valence state of 4 with four $2sp^3$ orbitals that are all accounted for by hybridization. The $2sp^3$ orbitals are bonded to other carbon atoms through strong covalent bonds to form a tetrahedron structure with equal angles to each other of 109°2.8 shown in Figure 2.2.

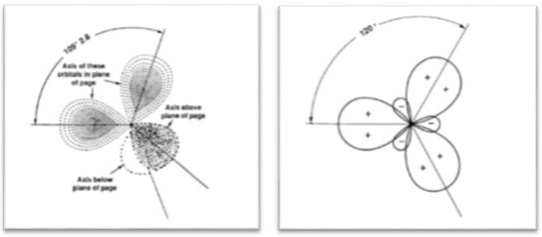

Figure 2.2: Left: Tetrahedral hybridization of the sp3 orbitals with the negative lobes omitted. Right: Planar section of sp2 hybrid orbitals of the carbon atom [2].

The sp^3-tetragonal hybrid orbital is one of three orbital configurations for carbon atoms that accounts for the various carbon allotropes and compound symmetries. The other two orbitals are the sp^2 and sp orbitals. The sp^3 orbital is the key to diamond and aliphatic compounds whereas for all graphitic structures and aromatic compounds, the sp^2 orbital is the key.

The hybridization mechanisms for sp^2 and sp^3 orbitals are slightly different from one another. Unlike in the sp^3 hybridization mechanism, the electrons in the L shell of the ground-state atom are rearranged in such a way that one $2s$ electron is moved to be combined with two of the $2p$ orbitals. They form three sp^2 orbitals and a delocalized p orbital electron. The electron-density contour of the two orbitals is similar in shape and can be seen in Figure 3. Both sp^2 and sp^3 orbitals are directional and referred to as sigma (σ) orbitals and form a sigma bonds. The three sp^2 orbitals are identical and are on the same plane with their orientation of maximum probability forming at equal angles of 120° as shown in Figure 2.2.

The fourth orbital, the delocalized p orbital electron, is directed perpendicular to the plane of the three sp^2 orbitals and becomes available to form a subsidiary pi (π) bond with the other atoms [2] [3].

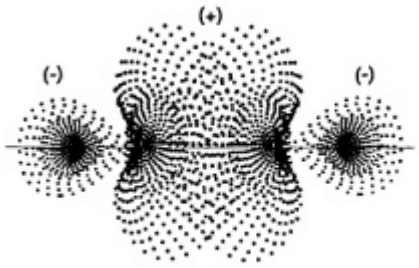

Figure 2.3: The sp3 hybrid orbital bonding (sigma bond) showing covalent bonding [2].

This chapter will further discuss the various properties and synthesis of diamond.

2.2 Properties of Diamond

Diamond is a semiconductor with the most superior physical, chemical and electrical properties of all semiconductors. These properties include its high thermal conductivity ($10 - 20\ W/cmK$), ultra-hardness, wide transparency (from ultraviolet to infrared light), radiation hardness (extremely resistant to neutron radiation), breakdown electric field of 10 M/cm, unusually high refractive index and a low dielectric constant of 5.5 [2] [24] [25]. Diamond is one of the most important allotropes of carbon with a giant molecular structure of carbon atoms that form directed sp^3 covalent bonds [26]. Since covalent bonds are strong, they require a lot of energy to separate each atom, which in turn results in very high melting $(3350)^{\circ}C$ and boiling $(4830)^{\circ}C$ points [27]. Due to its molecular structure, diamond is the hardest known material thus far. The properties of diamond are summarized in Table 2.1.

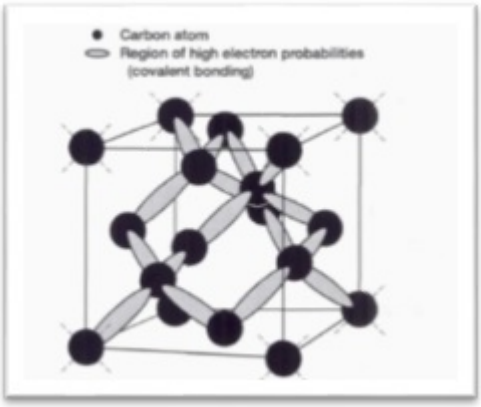

Figure 2.4: 3-Dimensional representation of sp3 covalent bonding, lattice structure of a diamond [3].

Table 2.1: Properties of Diamond [28].

Lattice Structure	Cubic
Lattice Constant (RT)$[Ang]$	3.567
Atomic Density $[cm^{-3}]$	1.77×10^{23}
Specific Gravity $[g/cm^3]$	3.515
Thermal Conductivity (RT) $[W/cm \cdot K]^b$	≈ 25
Debye Temperature $[K]$	1860
Bulk Modulus $[N \cdot m^{-2}]$	$4 - 5.5 \times 10^{11}$
Elastic Moduli $[GPa]$	–
Band gap $[eV]$	5.47
Electron Mobility (RT) $[cm^2/(Vs)]$	1800
Hole Mobility (RT) $[cm^2/(Vs)]$	1500
Dielectric constant (RT, low freq.)	5.58
Breakdown field $[V/cm]$	10^7
Refractive Index (in the visible)	2.4
Melting Point $[K]$	4500
Thermal expansion coefficient at RT $[/K]$	$\approx 1 \times 10^{-6}$
Velocity of Sound $[cm/s]$	$\approx 1.96 \times 10^5$
Raman Frequency $[cm^{-1}]$	1332

^{b} Highest reported value.

Diamonds can be classified according to their optical absorption properties which are determined by the impurities found within the structure. A summary of the different classes of diamond is given in Table 2.2. The first class is type Ia diamonds, these type of diamonds consist of up to 0.1 % nitrogen impurities that are distributed inhomogeneously within the dia-

Table 2.2: Summary of different types of diamond [2].

Type	Origin	Impurities
Ia	98 % of all natural diamonds.	Approximately 0.1 % nitrogen impurities in small aggregates.
Ib	Approximately 0.1 % nitrogen high-pressure synthetic diamonds.	Nitrogen impurities of 0.05 %.
IIa	Rare in nature.	Few ppm of nitrogen and is usually clear.
IIb	Extremely rare in nature. Produced by high-pressure synthesis.	Less nitrogen than IIa.

mond structure. These exhibit very strong absorption in the infrared and are not paramagnetic. Type Ib diamonds contain nitrogen as substitutional impurities. These are rare to find in nature as most of the time the nitrogen is implanted into the diamond structure through high pressure synthesis. They have a nitrogen content of approximately 0.05 % in the lattice and they exhibit some form of paramagnetism.

Type IIb diamonds are naturally boron-doped, these are extremely rare in nature and are most commonly produced by high pressure synthesis. It becomes a semiconductor when doped by boron and usually appears blue. They show p-type conductivity due to an acceptor level that is introduced by the substitutional boron located $\approx 0.35eV$ above the valence band. Lastly we have type IIa diamonds, these are the most pure form of diamonds and rare to find in nature. They consist of a few parts per million (ppm) nitrogen content in their structure. They exhibit the intrinsic semiconducting properties of diamond with a wide bandgap of $5.5eV$ and an extremely high carrier mobility (≈ 2200 and ≈ 1600 cm^2/Vs for electrons and holes respectively [24]). They therefore possess exceptional properties that could find applications in high-power microwave electronics, microelectronics, microelectromechanical system (MEMS) technology, substrates, high temperature and high power electronics, ultraviolet light-emitting diodes and optics [2] [25] [28].

2.3 Diamond Synthesis

Diamond can be separated into four categories namely: natural diamond, high-pressure synthetic diamond, chemical vapour deposition (CVD) (vapour phase) diamond and diamond-like carbon. Natural diamond was first reported over 2700 years ago in India. They are produced under very high pressures and temperatures like volcanic shafts. To shorten the production of diamond; a French chemist, A. L. Lavoisier, discovered in 1722 that the

product of diamond combustion is singular, i.e. resulted in carbon dioxide. Years later, in 1814, an English chemist H. Davy also confirmed that burning diamond produced carbon dioxide. He concurrently proved that diamond was a crystalline form of carbon. Over the centuries, scientists attempted to duplicate natural diamond through synthesis and it was only in 1955 that the United States, Sweden and the Soviet Union were able to synthesize diamond [2] [3]. Synthetic diamond has many applications in industry and there are various methods used to synthesize diamond. These methods include high pressure-high temperature (HPHT) synthesis, detonation of explosives, laser ablation, graphite etching and chemical vapor deposition (CVD) [29]. In this section, the HPHT-synthesis method will be discussed.

- **High Pressure-High Temperature (HPHT) synthesis**
  The high pressure-high temperature synthesis method is one of the popular synthesis methods. This methods tries to duplicate the natural process of diamond formation. There are various processes in which high pressure diamond can be synthesized, it can either be through graphite-diamond transformation, solvent-catalyst high pressure synthesis or shock-wave processing.

  The Graphite-Diamond Transformation
  The transformation of graphite to diamond is a rather important process in contrast to the diamond-graphite transformation which is mostly of academic interest. Graphite can be transformed into diamond under high pressure and temperature. From extensive thermodynamic data, the transformation can be expressed using the following equation:

$$P^{(eq/atm)} = 7000 + 27T(orT > 1200K) \tag{2.1}$$

  where $P^{(eq/atm)}$ is the pressure measured in atm and T is the temperature measure in kelvin (K) [2]. Some of the thermodynamic data considered in PT relationship include the heat formation of graphite-diamond, the heat capacity of graphite as a function of temperature and the atomic coefficient of thermal expansion of diamond. The PT relationship is shown in Figure 2.5, where the equilibrium line shows the separation between graphite and diamond, and the shaded region shows where graphite is transformed into diamond.

  The graphite-diamond transformation is thermodynamically feasible at relatively low pressures and temperatures, this is illustrated in Figure 2.6. Unfortunately this transformation faces a kinetic barrier since the rate of transformation decreases with increasing pressure. To observe direct graphite-diamond transformation, the thermodynamic

conditions favourable for this process were experimentally determined to be at an extremely high pressure and temperature ($> 130\ kb$ and $> 3300\ K$) [2] [4] [30]. Unfortunately these conditions are not very easy to achieve but luckily the solvent-catalyst reaction can be used instead to by pass the kinetic barrier.

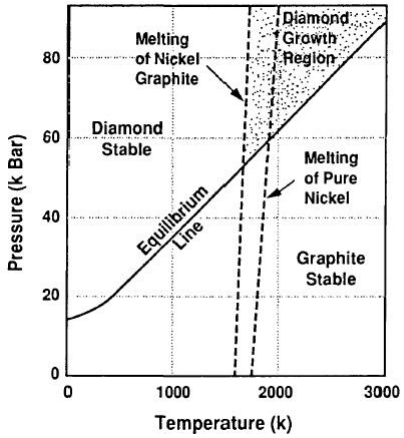

Figure 2.5: Pressure-temperature diagram of diamond-graphite with melting lines of nickel and nickel-graphite eutectic [2].

Solvent-Catalyst High-Pressure Synthesis
The solvent-catalyst reaction establishes a reaction path that has a lower activation energy than that of a direct graphite-diamond transformation. This allows the process to occur faster than a direct transformation resulting in the solvent-catalyst synthesis being readily accomplished and now a viable and successful industrial process.

To obtain the required pressure, the hydraulic process is used. In this process, a hydraulic press is used to apply pressure with tungsten-carbide pistons. The cell is electrically heated such that the nickel melts at the graphite interface where the diamond crystals start to nucleate. A thin film of nickel separates the graphite and diamond, as the diamond crystals grow, the graphite is gradually depleted until there is no graphite left.

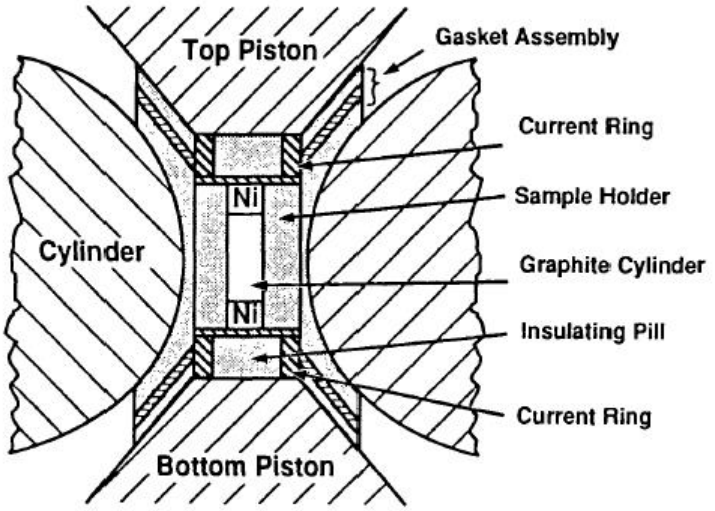

Figure 2.6: High-pressure cell for the production of diamond [2] [4].

Shock-Wave Processing
Another process in which HPHT-diamond can be synthesized is through shock-wave processing where a high pressure is generated by shock waves from an explosion. The explosion produces direct conversion of graphite into diamond. This process is illustrated in Figure 2.7 where a mixture of graphite and nodular iron is placed inside a cavity in a lead block. A flat plate coated with explosives on the back is placed on the front of the cavity. The explosives are detonated and gives the plate initial velocity of approximately 5 km/s before impact with the cavity. For a few microseconds, the peak pressure and temperature are estimated to be 300 $kbar$ and 1000 K respectively. The presence of an iron solvent-catalyst assists in the formation of diamond. The diamond crystals are then separated through acid digestion and sedimentation.

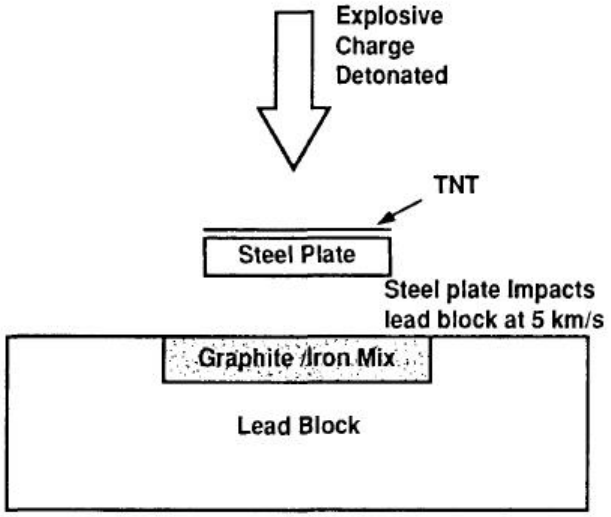

Figure 2.7: Schematic of shock-wave processing of diamond [2].

2.4 Ion Implantation of Diamond

Ion implantation is a technique which enables one to introduce impurities into the near surface of a solid. In this section, we focus on ion implantation in diamond. During ion implantation, various processes and parameters are considered. The energy loss process that the incoming energetic ions undergo is discussed in slight detail together with the parameters that are considered during ion implantation. Finally, the implantation-induced damage in diamond is discussed.

Energy-Loss Mechanisms:
When an energetic ion penetrates through a solid, the ion loses energy through scattering events. The scattering events involve Coulomb interaction of the ion with the atoms and electrons of the target. The energy loss is an important factor in determining the final penetration depth of the ion and the amount of disorder caused within the lattice of the target.
Every collision that occurs between the ion and the constituents of the target is a complicated many-body event explained by a complicated Hamiltonian. The Hamiltonian can be approximated by assuming that the interaction between the ion and the constituents of the target is separated into two components, namely an ion-nucleus interaction and ion-electron interaction. The energy loss of the incident ion can be divided into two dominant mechanisms, namely the electronic energy loss which involves the interaction between the incident ion and electrons of the target material, and the nuclear energy loss which involves the interaction between the incident ions and

the atoms of the target material.
The slowing down of an ion in matter can be treated using the stopping power defined as (dE/dx) where dE is the energy loss of the ion traversing a distance dx. The stopping power can be expressed as:

$$dE/dx = N \int T d\sigma \tag{2.2}$$

where $d\sigma$ is the cross section of the collision, T is the energy loss of the ion during the collision event and N is the density of the scattering centre of the target material. The stopping cross section can thus be defined as:

$$\varepsilon = 1 dE/N dx = \int T d\sigma \tag{2.3}$$

The total stopping power mentioned above is a result of the summation of the electronic and nuclear processes and can be expressed as:

$$dE/dx = (dE/dx)_e + (dE/dx)_n = N(\varepsilon_e + \varepsilon_n \tag{2.4}$$

where ε_e and ε_n are the electronic and nuclear stopping cross sections, respectively [28].
The Lindhard-Scharff-Schiott (LSS) theory for ion implantation in solids by Lindhard et al. [31] gives a detailed description of the electronic energy loss. The LSS theory approaches the electrons in the target solid as free electron gas that are affected by the traversing positive charge of the ion. The moving ion introduces an inhomogeneity in the electron plasma, this induces a stopping force on the ion and therefore causes a loss in the energy of the ion. The theory allows the prediction that the electronic stopping power is proportional to the ion velocity, i.e. $(dE/dx)_e$ is proportional to $\sqrt{E}$ for ion velocities of relevance to the ion implantation.

The interaction between the ion and the nucleus is given by the Coulomb interaction between two positive charges that result in both energy loss and change in trajectory of the ion. The Rutherford scattering cross section explains the cross section of the process. For the ion-nucleus interaction, the colliding ions do not only change directions but the atoms of the target material are significantly misplaced and hence resulting in lattice defects. In summary, it can be concluded that the deviations in the ion trajectory results in both a lateral spread and depth distribution of implanted ion species, while the displacements of atoms in the target material results in lattice damage [28].

Parameters of Implantation:
The energy loss of the incoming ion is not the only factor that needs to be considered when implanting ions into solids. A number of parameters are

taken into account like the ion species, its energy E_0, ion range R, the mean projected range R_p, the projected range straggling $\triangle R_p$, the fluence ϕ, and the flux, also known as the beam current i_b.

The interaction between ion beams and target materials depends on the energy, mass, charge of the incident ion and properties of the target material. Various implantation processes occur depending on the energy of the incident ion. For low energies ($\backsim 10 - 100eV$), the ions come to rest within a few atomic layers. These energies can be used for ion beam deposition processes where ions are implanted on the surface of the target material. At slightly higher energies ($1\ keV$), heavy ion beams are used for sputtering purposes. For incident ions with energies in the range $\backsim$ 10 - $300keV$, the ion implantation process is used to modify the properties of carbon-based materials to a penetration depth of $10^2 - 10^4$ angstroms depending on the mass of the ion species and target density. The study of the distribution of chemical constituent and lattice disorder is made possible by light ions with energies above $\backsim 300keV$ [28].

The implantation range is in the order of 1000 - 3000 Angstroms and therefore ion implantation can be considered as a near surface phenomenon. The projected mean range R_p is the actual quantity used to define the position of the peak, measured from the surface of the target and with the corresponding half-width at half maximum $\triangle R_p$ of the implant distribution. Extrinsic parameters that also affect the implantation process are the ion fluence and the beam current. The ion fluence is the total number of incident ions per unit area of the target material. Depending on the number of incident ions per unit area, the ion fluence can be used to modify the electronic or optical properties and structural modifications.

Implantation-Induced Modifications to Diamond:
Implantation-induced modification to diamond results in structural and damage - related electrical conductivity, volume expansion, lattice damage, damage annealing and implantations at elevated temperatures, electrical doping, impurity-state identification and electronic-device realization. In this subsection, the lattice damage as a result of ion implantation will be discussed.

In most crystalline structures, along certain directions, holes exists referred to as tubular holes that allow beams of ions to travel long distances within the crystal with no high angle collision occurring. This is known as the "channeling effect" and can be utilized to investigate properties of the crystal lattice and the perturbations of crystals like doping in the bulk region that cannot be accessed by x-rays [32]. Channeling experiments can give direct information on the lattice damage caused in diamond from light ions such as hydrogen (H) and helium (He).

The simple structure of crystalline diamond and its high Debye temperature [28], allows for the channeling effect to be very effective with extremely good channels found within diamond. Damage caused to diamond from room-temperature implantation indicates a distinctive peak in the backscattered particle spectrum that indicates a close correlation between the depth and implantation range. The peak appears to grow with an increase in implantation dose until a certain level is reached, further implantation will lead to the broadening of the damage peak which at high doses will extend from the crystal depth to a depth of roughly $R_p + \triangle R_p$. Much of this damage is attributed to graphitization, where small graphite structures are formed on the surface of the diamond structure [28].

Chapter 3

Magnetism

In this chapter, various types of magnetism and how they behave in carbon structures are discussed. Diamagnetism is the most common type of magnetism found in carbon structures and it is therefore be discussed first followed by paramagnetism, ferromagnetism and superparamagnetism.

3.1 Diamagnetism

Diamagnetism is a type of magnetism where all the electrons in an atom of a material are paired. In other words, the material is non-magnetic. Diamagnetic materials have closed shell electronic structures and result in no net magnetic moment. In 1905, Paul Langevin formulated the classical theory of diamagnetism and from this theory he showed that diamagnetism has a negative susceptibility (χ) [33].

According to the Pauli Exclusion Principle, electrons in the same orbital can never have the same spin quantum number. As a result, when two electrons are paired together in an orbital they will have a total spin of zero. This is the reason why diamagnetic atoms do not have a net magnetic moment. Considering the orbital motion of electrons, we notice that there are tiny current loops. These current loops produce magnetic moments that tend to align themselves under an applied field in such a way that they oppose the applied magnetic field. This phenomena is basically the atomic view of Lenzs law that states "when the flux through an electrical circuit is changed, an induced (diamagnetic) current is setup in such a direction as to oppose the flux charge" [34] or in simpler terms "the induced magnetic fields tend to oppose the change which created them" [35]. Materials that exhibit this kind of behaviour in the presence of a magnetic field are categorized as diamagnetic materials.

Diamagnetism in Carbon

It is a known fact that carbon and all its allotropes are diamagnetic. Considering the common allotropes of carbon like graphite, diamond, fullerenes and carbon nanotubes; we notice that different interactions are considered to determine the magnetic susceptibility. Diamond and graphite are used as examples to explain diamagnetism in carbon structures. The diamagnetism of diamond can be described by a simple model that is based on the magnetic contributions of localized electrons while for graphite on the other hand, its diamagnetic susceptibility is anisotropic. The simple model used to describe the diamagnetism of diamond is adopted from the theory of diamagnetism by Paul Langevin. The classical result determined by Langevin is expressed as:

$$\chi = (\mu_0 N\mu)/B = (\mu_0 NZe^2)/6m < r^2 > \tag{3.1}$$

where N is the number of atoms per unit volume and $< r^2 >$ is the electron distribution within the atom [34]. The result follows from his theory which states that "Negative magnetism is present in an applied field even though the material is composed of atoms that have no net magnetic moment" [33]. The magnetic contributions of localized electrons is the sum of two Langevin diamagnetic terms $\chi_{(c)}$ and $\chi_{(v)}$ which are known as the core and valence electrons respectively, and a Van Vleck paramagnetic susceptibility denoted as $\chi_{(vv)}$. The Van Vleck term is a result of the transitions of virtual magnetic dipoles between the valence band and the conduction band (or in simple terms: between the filled and empty energy levels [10]). The absence of states at the Fermi level results in the non-consideration of the Landau diamagnetism (χ_L) and Pauli paramagnetism (χ_p) when determining the final diamagnetic susceptibility of diamond. It is important to note that the magnetic moment of diamond is temperature independent, this information will be useful in the interpretation of the results later on.

From literature, it is reported that the magnetic susceptibility of various carbon structures is strongly dependent on the presence or absence of an aromatic-like π - electrons. The presence or absence of these aromatic-like π - electrons results in carbon structures having different diamagnetic susceptibilities. A summary of magnetic susceptibility of various carbon structures/ allotropes is given in the introduction. Table 3.1 clearly shows the significance of the aromatic-like π-electrons through the variance of diamagnetic susceptibilities.

Table 3.1: Diamagnetic susceptibilities of carbon allotropes [1].

Carbon Allotrope	Diamagnetic Susceptibility ($\chi - emu/g$)
Diamond	-4.9×10^{-7}
Graphite - parallel to the plane	-5×10^{-7}
Graphite - along the c-axis	-30×10^{-6} below $100K$
C_{60}	-3.5×10^{-7}
C_{70}	-5.9×10^{-7}

Figure 3.1 shows diamagnetic susceptibilities of more carbon structures like HOPG, graphite rods, SWNH's and MWNT's. These are experimental values reported in literature. The values were measured with change in temperature to observe and confirm that the diamagnetic susceptibility of a carbon structure is invariant of temperature.

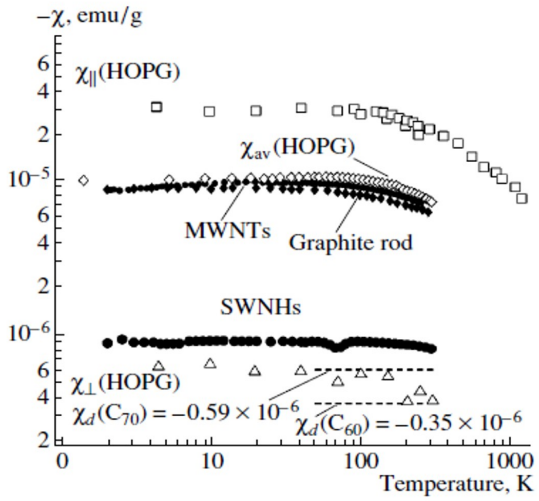

Figure 3.1: Diamagnetic susceptibilities of carbon structures [5].

3.2 Paramagetism

Paramagnetism is the opposite of diamagnetism and therefore has a positive magnetic susceptibility. The positivity of the magnetic susceptibility implies that an applied magnetic field will induce magnetization in materials. Paramagnetic materials consists of atoms with non-zero magnetic moments, i.e. atoms with unpaired electrons. The magnetic moments in a paramagnetic material are all assumed to be independent, i.e. isolated magnetic moments. Due to the weak interaction between the magnetic moments of the neighbouring atoms, the magnetic moments are in random directions. When a magnetic field is applied, the magnetic moments are aligned to some degree

depending on the strength of the field applied. The alignment of the moments induces magnetization [6].

A short review of the quantum theory of paramagnetism is discussed below to better explain the phenomenon. Consider first the magnetic moment of an atom in free space, expressed as:

$$\mu = \gamma \hbar J = -g\mu_B \tag{3.2}$$

(This follows from $\mu_B = -\gamma\hbar$, where γ is a constant expressed by: $\frac{e}{2m_e}$) where J is the total angular momentum, i.e. the sum of the orbital (L) and angular (S) momenta. μ_B is the Bohr Magneton and g is the g-factor, as known as the spectroscopic splitting factor. The Bohr magneton is defined by: $\mu_B = e\hbar/2m$, this value is almost equal to the spin magnetic moment of a free electron. Next we consider the energy levels of a system in a magnetic field, expressed as:

$$E = \mu \cdot B = m_j g \mu_B B \tag{3.3}$$

where m_j is the azimuthal quantum number and takes the values of $J, J - 1, , -J$. If we consider a single spin with no orbital moment then the values for m_j are $\pm 1/2$ and since we know the g- factor value for an electron spin is $g = 2$, we can express the energy levels of the system as:

$$E = \pm \mu_B B. \tag{3.4}$$

An illustration of the energy levels is shown in Figure 3.1. The diagram shows the energy level splitting for a single electron in a magnetic field B which is directed along the positive z-axis. For an electron, the magnetic moment μ acts in opposite direction to the spin S and hence we have $\mu = -g\mu_B S$. In the low-energy state on the other hand, the magnetic moment is parallel to the magnetic field [34].

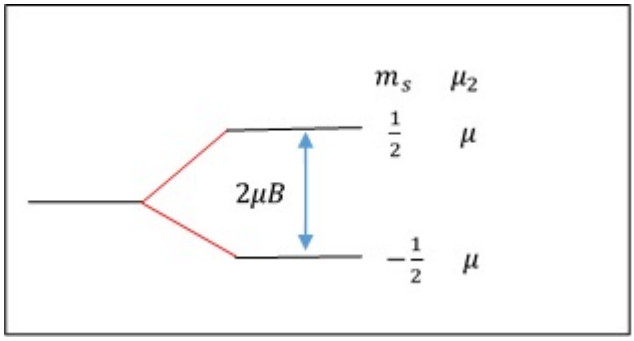

Figure 3.2: Energy level splitting of an electron.

Looking at the equilibrium population for a two level system, we notice the following:

$$N_1/N = e^{(\mu B)/(k_B T)}/e^{(\mu B)/(k_B T)} + e^{(-\mu B)/(k_B T)} \tag{3.5}$$

$$N_2/N = e^{(-\mu B)/(k_B T)}/e^{(\mu B)/(k_B T)} + e^{(-\mu B)/(k_B T)} \tag{3.6}$$

The total number of atoms N is given by $N = N_1 + N_2$ =constant where $N_1 + N_2$ are the lower and upper levels respectively. The total number of atoms is constant following the laws of Conservation of Matter. The resultant magnetization for n atoms per unit volume of the system is given by:

$$M = (N_2 - N_1)\mu = N\mu(e^x - e^{-x})/(e^x + e^{-x}) = N\mu \tanh(x) \tag{3.7}$$

where $x = \mu B/(k_B T)$, this expression is used for the special case, $J = 1/2$. If we consider the case were $x \ll 1$ then $\tanh(x) \approx x$ and the magnetization will be given by:

$$M = N\mu x = N\mu(\mu B/(k_B T)) \tag{3.8}$$

This expression is known as the Curie-Brillouin Law [33]. Focusing on an atom with an angular momentum quantum number J that is placed in a magnetic field, then the atom has $2J + 1$ equally spaced energy levels. The magnetization is given by:

$$M = NgJ\mu_B B_j(x) \tag{3.9}$$

with $x = gJ\mu_B B/k_B T$ where B_j is the Brilloiun function defined by:

$$B_j(x) = (2J + 1)/2J \coth((2J + 1)x/2J) - 1/2J \coth(x/2J) \tag{3.10}$$

The case for $x \gg 1$ is better illustrated in the diagram below.

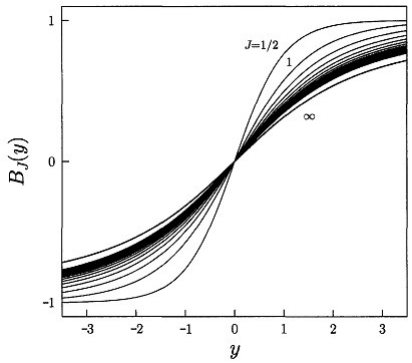

Figure 3.3: Magnetization of a paramagnet for various values of J that follow the Brillouin function B_j [6].

For $x = \mu B/(k_B T) \ll 1$ then we have $\coth(x) = 1/x + x/3 - x^3/45 +$, and the susceptibility is given by:

$$M/B \approx (NJ(J+1)g^2\mu_B^2)/(3k_BT) = (Np^2\mu_B^2)/(3k_BT) = C/T \qquad (3.11)$$

This is the Curie Law where p is simply the effective number of the Bohr magnetons and defined as $p \equiv g[J(J+1)]^{1/2}$ and C is the Curie constant [34]. Since paramagnetism has various origins, there are different types of paramagnetism namely: Curie paramagnetism, Curie-Weiss paramagnetism, Pauli paramagnetism and Van Vleck paramagnetism. In order to determine the type of paramagnetism a material exhibits, the magnetization as a function of applied magnetic field ($M(H)$) curve is used. The origin of paramagnetism in a material is determined using the magnitude of χ and the temperature dependence of the susceptibility $\chi(T)$.

The Curie-type paramagnetism is the type of magnetism that arises from the presence of atoms with unpaired electrons. Within a Curie-type paramagnet, there is a force that tries to align the magnetic moments of the atoms with the magnetic field applied. This type of magnetism has a temperature dependence that can be expressed as: $\chi(T) = C/T$ where C is a constant known as the Curie constant defined above. The Curie temperature dependence of the material is a result of the tension that is between the force trying to align the magnetic moments parallel to the applied field and the tendency of the heat trying to disrupt the alignment. As the temperature is increased, the relative effect of the field decreases. A very useful technique to characterise Curie-type paramagnetism is to plot $1/\chi$ versus T, this should give a straight line where $1/C$ will be the slope of the curve. The Curie constant can be used to determine what the product of the effective magnetic moment of an atom is and the number of magnetic atoms present.

For the Curie-Weiss paramagnetism, there is not only an interaction with the applied magnetic field, but there is also an interaction between the magnetic moments on the different atoms. The interaction between the magnetic moments is known as the exchange interaction. Exchange interaction is a quantum mechanical effect that occurs between two identical particles. This effect occurs when the wave function of identical particles is subjected to exchange symmetry, the wave function will either remain unchanged or its sign changes. The exchange of the moments can either align adjacent moments in the same direction or it can align the neighbouring moments in opposite directions. The Curie-Weiss magnetic susceptibility can be expressed as:

$$\chi_{CW} = C/(T - \theta) \qquad (3.12)$$

where θ is the Curie-Weiss temperature. This temperature is related to the strength of the interaction between the moments, the sign of the temper-

ature is dependent on whether the interaction is aligning moments in the same direction or in opposite directions. When $\theta > 0$ then the interaction aligns the adjacent moments in the same direction and from this one can conclude that there is a net ferromagnetic interaction between the moments. When $\theta < 0$ then the interaction aligns the neighbouring moments in the opposite direction and from this one can conclude that there is a net anti-ferromagnetic interaction between the moments. To characterise the Curie-Weiss paramagnetism, the same plot as that of the Curie-type paramagnetism can be plotted. Unlike in the Curie-type paramagnetism where the straight line goes through the origin, the Curie-Weiss either intercepts through the positive or negative x-axis (temperature). For $\theta > 0$, the line intercepts through negative temperature and for $\theta < 0$, the line intercepts through the positive temperature.

Pauli paramagnetism can be observed in metals. In metals, the conduction electrons have magnetic moments that can be aligned when a magnetic field is applied. The magnetic susceptibility in Pauli paramagnetism is nearly independent of temperature and very small in most cases. The last of the types of paramagnetism is the Van Vleck paramagnetism. The Van Vleck paramagnetism can be associated with the thermal excitations of low-lying states. This type of paramagnetism is nearly independent of temperature as well and usually has a small magnetic susceptibility value [7].

Paramagnetism in Carbon

Paramagnetism is reported by Esquinazi et al. in a letter titled "Magnetic properties of ion-implanted diamond" published in Diamond and Related Materials [18]. In this letter they report a paramagnetic signal that was observed using the superconducting quantum device (SQUID). Since crystalline type IIa diamond was implanted with boron ions and chemically deposited diamond was implanted with fluorine or iron ions. The structural properties of the boron-doped diamond samples were studied using Raman Spectroscopy and all magnetization measurements were performed using the SQUID. From the magnetization measurements, all samples show that their magnetic properties are dominated by the diamagnetic signal of the diamond that superimposes the paramagnetic signal which is observed in the fluorine- and iron-implanted samples.

The room temperature fluorine- and iron-implanted ions in the diamond samples produced lattice disorders and enhancements in the paramagnetic centres. The disorder produced lead to a paramagnetic contribution in the magnetization, this contribution increased with an increase in implanted ions. The boron implanted diamond samples produce less lattice disorders and almost no paramagnetic signal was observed [36]. A ferromagnetic like signal was observed but dismissed due to artefacts that may have been

detected by the SQUID.

3.3 Ferromagnetism

In a ferromagnetic material, the atoms have a net magnetic moment just like those found in paramagnetic materials. However, unlike paramagnets, the magnetic moments in ferromagnetic materials tend to align with each other spontaneously in the absence of an applied magnetic field; this implies that they possess a permanent magnetic moment in the absence of an externally applied magnetic field. The alignment of the moments form magnetic domains which are a consequence of the Pauli exclusion effect that predicts the existence of an exchange energy. This exchange energy induces the neighbouring electron spins to align, overcoming their classical tendency to anti-align. As the distance between the moments increases, the exchange energy is reduced and therefore results in magnetic domains that are anti-aligned.

When a ferromagnetic material is placed in an external magnetic field, the magnetic domains which are aligned with the field are increased and those opposing the field are decreased. This effect is not reversed when the magnetic field is removed and hence the material retains its magnetism, this effect is known as a hysteresis loop or magnetic hysteresis. A hysteresis loop is the behaviour observed on magnetization curves as a function of applied field $M(H)$ and as a function of temperature $M(T)$. In Figure 3.3, a diagram of the magnetic flux density versus the magnetic field strength of a ferromagnetic material is shown. The material is subjected to forward and reverse saturations indicated by S and $S^{'}$ respectively. The hysteresis loop is represented by the red solid line and the dashed blue line represents the initial magnetization. B_r and H_c represents the remanence field and the coercive force respectively.

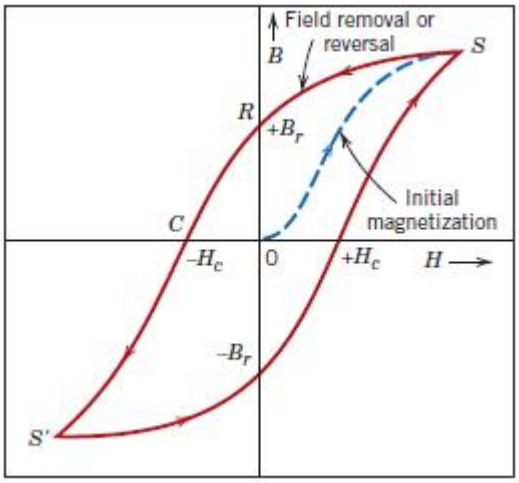

Figure 3.4: Magnetic flux density versus the magnetic field strength [7].

Figure 3.3 shows that as the magnetic field strength, H, is increased the magnetization also increases gradually until it reaches a maximum value known as the saturation magnetization and is denoted by S in the figure. As H is decreased from the maximum value, a different curve is followed but on the way down the magnetization does not stop at zero when H reaches zero. Instead it continues all the way down to the minimum value of the magnetization denoted by S. The value of the magnetization when H is zero is referred to as the remanent magnetization. The remanent magnetization is denoted by B_r and is used to classify soft and hard ferromagnets. To return the magnetization of a ferromagnet to zero, a sufficiently large magnetic field acting in the opposite direction should be applied. This field is known has the coercive field/force and denoted by H_c [7].

Ferromagnetism is the direct influence of two quantum phenomena, spin and the Pauli Eclusion Principle. Since the intrinsic spin angular momentum of an electron has a magnetic dipole moment associated with it, a magnetic dipole moment is created. In many materials that have filled electron shells, the electrons normally come in pairs of opposite signs and they cancel each others dipole moments out. Only materials with unpaired electrons will experience a net magnetic moment from a spin. Ferromagnetic materials consists of unpaired electrons and when they are aligned, they create a measurable macroscopic field. As already stated, paramagnetism is when spins/dipoles align parallel to an applied external magnetic field. Ferromagnetism in the other hand, involves an additional phenomenon where the spins align spontaneously in the absence of an applied field. This effect is purely quantum mechanical.

If the temperature is increased in a controlled environment, the thermal oscillation or entropy of the ferromagnet will compete with the ferromagnetic tendency of the spins to align. When a certain temperature is reached, there is a second-order phase transition that occurs which causes the system to no longer maintain its spontaneous magnetization. The system will start to respond paramagnetically to an external field. The maximum temperature that is reached in order for this effect to occur is referred to as the Curie temperature and is known as the critical point where the magnetic susceptibility is theoretically infinite and there is no magnetization.

Ferromagnetism in Carbon

Experimental and theoretical results have been reported over the years where ferromagnetism has been observed. In 1968, N. Mutaga reported possible ferromagnetic states in hypothetical hydrocarbons. He stated that hydrocarbons with conjugate π-electron systems may show ferromagnetic spin alignment due to the topology of the molecular orbitals [12]. In 1989, S. Mizogami et al. reported ferromagnetic pyrolytic carbon. This ferromagnetism was achieved by using adamantane as a starting material and using the chemical vapour deposition (CVD) method under low temperature growth. In this paper they reported ferromagnetism at temperature $T = 10$ K with a saturation magnetization of $M_s = 0.5$ emu/g, a remanent magnetization of $M_r = 0.35$ emu/g, a coercive field of $H_c = 600$ Oe and a Curie temperature of $T_c = 400$ K [13]. Thereafter, macroscopic magnetic ordering phenomena in organic materials such as $p-NPNN(C_{13}H_{16}N_3O_4)$, $TDAE^{+}C_{60}^{-}(CN_2(CH_3)_2)_2^{+}C_{60}^{-}$ amorphous - like carbon and fullerene were also reported after performing various experiments [14] [15] [16] [17]. Other letters reporting ferromagnetism are from P. Esquinazi et al. titled "The role of hydrogen in room temperature ferromagnetism at graphite surfaces" and "Induced magnetic ordering by proton irradiation in graphite".

3.4 Superparamagnetism

Superparamagnetism is a special type of magnetic property that occurs in nanoparticles of specific sizes and smaller. The size of the nanoparticles can range from a few nanometers to around a tenth of a hundredth of a nanometer and can either be ferromagnetic or ferrimagnetic [37]. Superparamagnetism also describes the state of a single-domain-sized grain/nanoparticle that has sufficient thermal energy which overcomes barriers to reverse the magnetization [38]. They are referred to as single-domain particles due to the simple approximation as a result of the total magnetic moment of the nanoparticles being regarded as one giant magnetic moment that is composed of all the individual magnetic moments of the atom which form the nanoparticle. The barriers arise from various anisotropies which include

magnetocrystalline, shape, magnetoelastic and/or exchange anisotropy which are all proportional to the volume of the grain/nanoparticle. The magnetic anisotropy of a material imply that its magnetic behaviour is dependent on the direction, they can be distinguished accordingly:

- Magnetocrystalline anisotropy is a preference in direction from the atomic structure of the crystal,
- Shape anisotropy arises from particles that may not be completely spherical,
- Magneto elastic anisotropy arises from the tensions happening within the nanoparticles and/or,
- Exchange anisotropy arises from interactions that are between ferromagnetic and antiferromagnetic materials.

The probability that a spontaneous reversal will occur is dependent on whether or not the magnetization overcomes the energy barrier. The probability will be negligible when the energy barriers are large with respect to the thermal energy and hence the magnetization is blocked. On the other hand though, when the barriers have a relatively low thermal energy, thermal excitations will result in the reversal of the magnetization over very short time scales and the grain/nanoparticles will be in a superparamagnetic state. The superparamagnetic state will be discussed in more detail.

Nanoparticles with uniaxial anisotropy (nanoparticles that show preference for a certain direction, normally along which their magnetization aligns to) normally flip the direction of their magnetization randomly. This occurs due to the thermal energy of the energy barrier. The average time it takes for each flip to occur can be given by the relaxation time expressed as follows:

$$\tau = \tau_0 e^{(\Delta E/(k_B T))} \tag{3.13}$$

where τ_0 is the length of time characteristic to the material in question. This length is normally of the magnitude around $10^{-9} - 10^{-12} s$ [39], ΔE is the energy barrier that the magnetization flip has to overcome through thermal energy, k_B is the Boltzmann constant and T is the temperature. The equation above shows the connection between the average time between flips τ and the temperature T. The temperature between the blocked state and superparamagnetic state is defined as the blocking temperature and can be denoted as T_B. This has an implication that at the blocking temperature $T_B : \tau_m = \tau$ and is expressed as:

$$T_B = \Delta E/(k_B In(\tau_m/\tau_0)) \tag{3.14}$$

In order to observe the nanoparticles in their superparamagnetic state, the temperature and the energy barrier are not the only parameters involved but the measurement time (τ_m) should also be taken into consideration since each experimental technique has its own measurement time. One of two scenarios can occur depending on the measurement time:

$$\tau_m \ll \tau(T < T_B) : \tag{3.15}$$

This is the case when the average time that is between the flips is much larger than the time taken during the measurement. The particles are in a well-defined state usually referred to as the blocked state of the system. In this case, the temperature is less than the blocking temperature.

$$\tau_m \gg \tau(T > T_B) : \tag{3.16}$$

In this case, the average time between flips is much greater than the measurement time. This has an implication that the measurement observed is in a fluctuating state with the different unresolved magnetization. In the absence of an external field, the time-average net moment is measured to be zero. This is referred to as a superparamagnetic state and the temperature is greater than the blocking temperature. The implications that a superparamagnetic state has on a material is in the absence of an external field, the net moment will be zero. In the presence of an external field, the nanoparticles react in the same manner as a paramagnet with the exception that the magnetic susceptibility is much larger than that of a paramagnet (hence it is referred to as superparamagnetism). Superparamagnetism occurs below the Curie temperature and hence needs to be explained differently from ferro- and ferrimagnetism [39].

Chapter 4

Experimental Procedure

4.1 Apparatus

A number of instruments were used in order to fulfil the aims and objectives of the study. The Superconducting Quantum Interference Device (SQUID) was used for measuring very sensitive magnetic signals, the 5 MV tandem accelerator was used for the micro-irradiation of the sample, the magnetic field microscope (MFM) was used to characterise the irradiated area of the sample and Monte Carlo simulations were performed to estimate the radiation damage caused by vacancy production.

4.1.1 SQUID

The Superconducting Quantum Interference Device (hereafter referred to as SQUID) is used to measure very sensitive magnetic flux and output voltage signals [40]. The device can measure quantities such as magnetic fields, current, voltage, magnetic susceptibility and magnetic field gradients and converts them into magnetic flux.

The SQUID is a combination of flux quantization and Josephson tunneling. Flux quantization is a physical phenomenon; first predicted by F. London in 1950 and later experimentally observed by B. Deaver and W. Fairbank concurrently with R. Doll and M. Nbauer in 1961 [41]. In their experiment, they showed that the flux that is contained in a closed superconducting loop is quantized in units of quantum flux. The units are expressed using the following equation:

$$\Phi_0 = h/2e \approx 2.07 \times 10^{-15} Wb \tag{4.1}$$

where $h \equiv 2\pi\hbar$ is Plancks constant and e is the electronic charge. Flux quantization is the result of a single-valued macroscopic wave function moving

once around a superconducting loop expressed as:

$$\Psi(\overrightarrow{r},t) = |\Psi(\overrightarrow{r},t)|e^{i\varphi(\overrightarrow{r},t)} \tag{4.2}$$

In the absence of an applied field or current, the phase $\Psi(\overrightarrow{r},t)$ takes the same value throughout the superconductor for all Cooper pairs that have a charge of $2e$. In the case where a loop is threaded by a magnetic flux on the other hand, the phase around the loop changes by $2\pi n$, where n is the number of enclosed flux quanta [42]. The Josephson junction is a device found within the SQUID device. This junction is a result of the Josephson tunneling effect. The effect was first discovered by Brian Josephson in 1962 and later observed by Anderson and Rowell in 1963 [43]. The Josephson junction consists of an insulator that is sandwiched between two superconductors.

The tunneling effect is when electrons in a superconducting material form Cooper pairs that condensate into a shape that is of unique collective quantum waves. If the insulating material between the superconductors is very small (only a few nanometers) then the quantum waves manage to spill out of the superconductor, allowing electron pairs to go through the insulator. The movement of electrons from one superconductor to another creates an electrical current in the junction [44]. The total current that goes through a Josephson junction depends largely on the phase difference between the semiconductors. The phase difference is expressed as:

$$\delta = \theta_1 + \theta_2 \tag{4.3}$$

where θ_1 and θ_2 are arbitrary but fixed, hence the phase difference (δ) is also fixed [45]. The total current going through the junction is expressed as:

$$I_s(\delta) = I_0 sin\delta \tag{4.4}$$

known as the Josephson equation, I_0 is the maximum supercurrent (critical current). Small junctions have a critical current density expressed as:

$$j_0 = I_0/A_j \tag{4.5}$$

where A_j is the cross-section within the junction [42]. If the electrical potential across the Josephson junction is time-dependent then the phase difference (δ) will also be time-dependent and expressed as:

$$\delta(t) = \delta_0 + 1/\Phi_0 \int_0^t V(t')dt' \tag{4.6}$$

where $V(t)$ is the difference in potentials on both sides of the junction and Φ_0 is the flux quantization defined above. If $V(t) = 0$ then current $I_s(\delta_0)$ can

pass through the barrier/insulating material without any resistance. This is known as the DC (direct current) Josephson Effect. If the current is greater than the critical current (I_c), the junction will have a measurable resistance. If on the other hand, $V(t) = V(t') = V_0 = const$ then the DC current disappears and the voltage drops. The voltage drop generates an alternating supercurrent at a frequency defined by: $\omega = V_0\Phi_0$. This is known as the AC (alternating current) Josephson Effect [45]. In the SQUID device, there is a closed superconducting loop that includes either one or two Josephson junctions in the current path of the loop. Due to the quantized state of the superconducting ring and the extra-ordinary non-linear behaviour of the Josephson junction, the SQUID can resolve changes in the external magnetic field that approaches 10^{-15} teslas [7]. Measurements were taken using the MPMS XL (5T) system found at the Spanish National Research Council Institute - Consejo Superior de Investigaciones Científicas (CSIC) in Universidad Autónama de Madrdid (UAM). The system can apply a magnetic field of up to 50 kOe and the temperature ranges between 2 K and 400 K. Figure 4.1 shows a schematic diagram of the MPMS system and figure 4.2 shows an image of the system found in CSIC.

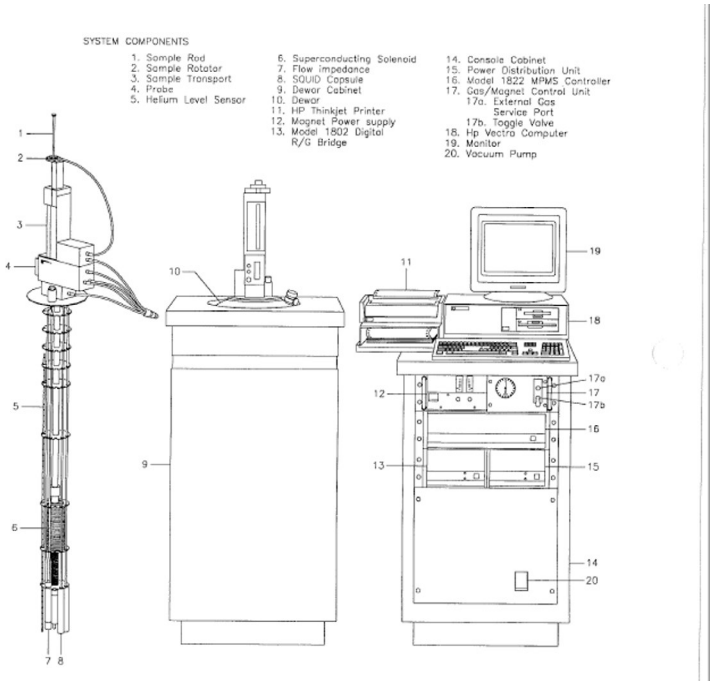

Figure 4.1: Schematic diagram of the MPMS XL (5T) system[8].

Figure 4.2: MPMS XL (5T) system at CSIC.

Every Magnetic Property Measurement System (MPMS) comprises of few principal components namely; the temperature control system, magnet control system, the superconducting SQUID amplifier system, sample handling system and computer operating system. The system superconducting SQUID amplifier system is the heart of the entire system. The MPMS system is dependent on the radio frequency (rf) SQUID detector; this detector is used to detect the magnetic moments of materials as the material is placed inside the sample chamber. The system provides the reset circuitry, autoranging capability, a highly balanced second-derivative sample coil array and electromagnetic interference (EMI) protection. Within the system, we find superconducting magnets, superconducting detection coils and the SQUID device itself. Each component is briefly discussed below.

A Superconducting Magnet
The superconducting magnet is used to generate large magnetic fields. This can be achieved with little or no electrical power due to its ability to support a very high current density with small to no resistance [46]. There are a number of things that have to be taken into consideration when working with superconducting magnets. For example, the relaxation time of the magnet and remanent field of the superconducting magnet.

After the field of the superconducting magnet has been changed, the magnetic field will decay. The decay is the relaxation the magnet undergoes in time and exhibits a logarithmic behaviour. When performing high-sensitivity measurements, it is important that the magnet gets enough time to relax before measurements are taken. This time can be determined from the size of the field since they are proportional to each other. The flux changes that are observed by the detection coil should come solely from the sample that is moving through the coil and not from the decay of the superconducting magnet.

The remanent field is the magnetic field that is trapped in the magnet after the magnet has been set to zero and should always be considered when working with superconducting magnets. The field is usually small relative to the maximum fields applied or available. Problems are only encountered

when working with low fields close to the remanent fields. It is therefore important to measure the fields so they can be taken into consideration when analysing the results. There are various ways in which the remanent field can be reduced, one way to do this is by lowering the field to zero using the oscillate mode instead of the persistent mode. This will lower the remanent field from the range of 1 to 20 Oe to a range of 1 to 3 Oe [47].

In the MPMS system, the superconducting magnet wound is employed in the solenoid configuration. The magnet is constructed in a closed superconducting loop which implies that the magnet is charged to a certain current and then can be operated without an external current source or power supply. The operation mode for the superconducting magnet is the persistent mode. To change the magnetic field in this mode, the closed superconducting loop needs to be opened electrically by using a persistent-current switch that is formed by wrapping a small heater around a short segment of the magnet's superconducting wire. When the heater is energized, the segment of the wire within the heater becomes normal and the closed superconducting loop is opened. By attaching a power supply to each side of the switch, it is possible to change the current in the superconducting magnet [7].

A Superconducting Detection Coil

The superconducting coil found in the MPMS system is a single piece of superconducting wire wound around a set of three coils configured as a second-order gradiometer. A second-order gradiometer is an extension of the first-order gradiometer. The configuration consists of the following, an upper coil is a single turn wound that goes clockwise. The centre coil consists of two turns wound that are counter-clockwise and the lower coil consists again of a single wound turn that is clockwise.

This configuration was designed to discriminate against constant field gradients, which is something that first-order gradiometers cannot do. Often, unwanted signals are not spatially homogeneous to a tolerable degree however, they do exhibit a gradient [48]. The configuration can be used to reduce the noise in the detection coil and also minimize the background drifts in the SQUID detection system. There are various causes that lead to the installation of the gradiometer coil; these include fluctuations caused by applying a large magnetic field from the superconducting magnet and also the relaxation in the magnetic field of the superconducting magnet. In the MPMS system, the detection coil is found at the centre of the superconducting magnet. The detection coil is located outside the sample chamber and in the centre of the superconducting magnet such that when the sample is moved through them, the magnetic field of the sample is coupled inductively to the coils.

A Superconducting Quantum Interference Device (SQUID)

As already mentioned, the SQUID is the most sensitive device available to measure magnetic fields which is what makes it the heart of the system. The SQUID uses the properties of the electron-pair wave coherence and Josephson junctions in order to detect very small magnetic fields. At the centre of the SQUID, there is a ring of superconducting material with one or more weak-links. Weak-links are weak electrical contacts between superconducting electrodes which exhibit direct (non-tunnel type) conductivity [**?**]. These weak-links have a critical current (I_c) which is much less than that of the main ring. A very low current density is produced, making the momentum of the electron-pairs small. Small momentum implies that the wavelength of the electron-pairs will be very long and therefore the phase difference (δ) will be less anywhere in the ring.

If a magnetic field (B) is applied perpendicular to the plane of the ring, a phase difference is produced in the electron-pair wave. The applied magnetic field will also induce a small current (I) that flows around the ring. This current produces a phase difference across the weak-links since the weak-links have a critical current less than that of the main ring. The current induced by the applied magnetic field is not sufficient enough to cancel out the flux in the hole. Since the phase of electron-pairs is not only dependent on the current density but also on the applied magnetic field, the quantum condition of the phase change around a closed path must be equal to $2\pi n$. The magnetic field produces a phase change around the ring that is expressed as:

$$\delta(B) = 2\pi\Phi_a/\Phi_0 \tag{4.7}$$

where Φ_a is the flux produced in the ring by the applied field [50]. Φ_a is not necessarily equal to an integral number of fluxons, this ensures that the total phase change is a multiple of 2π. The small current flowing around the ring also produces a small phase difference of $2\delta(I)$ across the weak-links. The total phase change is then given by:

$$\delta(B) + 2\delta(I) = 2\pi n \tag{4.8}$$

The phase difference produced by the circulating current can either add or subtract to the phase difference produced by the applied magnetic field. In most cases, it is energetically favourable to subtract, hence the current going in the anti-clockwise direction is denoted by I^- [49]. Using Josephsons equation and the equation of the phase change produced by the magnetic field around the ring, the magnitude of the circulating current ,I^-, is given by:

$$|I^-| = I_c \sin\pi(\Phi_a/\Phi_0) \tag{4.9}$$

As the flux in the ring is increased from 0 to $1/2\Phi_0$, the magnitude of the circulating current is increased to a maximum. As the flux is increased above $1/2\Phi_0$, the current is now energetically favourable to adding, changing to the clockwise direction denoted by: I^+ . By the time the flux has reached is maximum, (Φ_0), the magnitude of the circulating current is zero. A conclusion is reached that the circulating current has a periodic dependence on the magnitude of the applied magnetic field. The magnetic field has a period variation of Φ_0, which is a very small amount of magnetic flux. The ability of the SQUID to detect this effect enables it to be used as a high-sensitivity magnetometer [50]. The SQUID in the MPMS system does not detect the magnetic field directly from the sample but instead, the sample is moved through a system of superconducting detection coils that are connected to the SQUID. The coils are connected to the SQUID using superconducting wires, allowing the current from the detection coils to inductively couple the SQUID sensor. The SQUID electronics produce an output voltage that is proportional to the current flowing into the input coil of the SQUID, if properly connected. The SQUID device is located approximately 11 *cm* below the magnet which is found inside the magnetic shield. It functions as an extremely sensitive current-to-voltage converter.

As already mentioned, the measurement is performed by moving the sample through the detection coils. As the sample moves through the coils, the magnetic moment of the sample induces an electric current in the detection coils. Since the detection coils, connecting wires and the SQUID input coil form a closed loop, any change of magnetic flux in the detection coil results in a change in persistent current in the detection circuit which is proportional to the change in magnetic flux. Since the SQUID is a linear current-to-voltage converter, the variations of the current in the detection coils will produce corresponding variations in the SQUID output voltage which is proportional to the magnetic moment of the sample [7].

A superconducting magnetic shield

Due to the high-sensitivity of the SQUID, it is important for the sensor itself to be shielded from the fluctuations of the magnetic fields. These fluctuations can be a result of the ambient magnetic field of the laboratory as well as the large magnetic fields produced by the superconducting magnet. The magnetic shielding provided by the superconducting magnetic shield provides a volume of relatively low magnetic field in which the SQUID and its coupling transformers are located. In order for the SQUID to operate properly, the magnetic field in the shield must be stable. The superconducting magnetic shield is placed in the system to serve two purposes only:

1. To shield the SQUID detector from the magnetic field generated by the superconducting magnet and;

2. To trap and stabilise the ambient magnetic field present in the laboratory when the SQUID and the superconducting shield are first cooled to liquid helium temperature.

4.1.2 6 MV Tandem Accelerator

An electrostatic ion accelerator is housed at the Centre of Microanalysis of Materials (Centro de Microanálisis de Materiales (CMAM)), a research institute belonging to Universidad Autónama de Madrdid (UAM). The accelerator has a maximum terminal voltage of 5 MV and is used to perform analysis and modification of material studies. The research done at the facility ranges from Archaeometry, surface physics, photonics, basic ion matter interaction, solid state physics to energy related materials, biophysics, micro-patterning, nuclear physics, etc. A schematic diagram of the Tandetron accelerator system is shown in Figure 4.2. It is observed in the diagram that there are three principal components in the system before it splits into different beamlines.

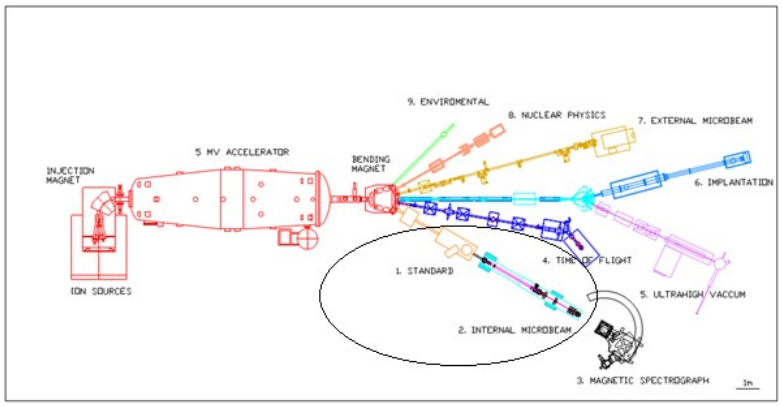

Figure 4.3: Schematic Diagram of the 5 MV Tandem Accelerator

These components are the injector configuration (ion sources and injection magnet), 5MV accelerator tank and the bending magnet. After going through the bending magnet, the beam splits into various beamlines to perform different experiments. These beamlines include; the standard beamline, the internal beamline, the nuclear physics beamline, the implantation beamline, surface physics beamline and lastly the time of flight beamline. For the experimental purposes of this research study, the standard and internal beamlines were used.

The standard beamline is in a vacuum and has a 4 axis goniometer. It consists of two charged particle detectors where one is fixed and the other

is movable. The movable detector makes it possible to vary the solid angle and change absorber foils. There is a high sensitivity optical camera and a special viewport which is used as a far-infrared (thermal) camera. It also consists of two gamma ray cameras namely $HPGe$ and $LaBr_3$ and optical quality viewports for ion beam induced luminescence (IBIL) and optical characterization. It can be used for classical ion beam analysis (IBA) techniques and ion beam modification of materials (IBMM) over small areas. The internal beamline consists of a $1\mu m$ beam size that has scanning coils for mapping irradiation for areas of up to $125 \times 125\mu m$. It can be used for IBA and IBMM for micro-patterning and single cell irradiation.

Now that we are familiar with the various beamlines, we can move on to the principal components of the Tandetron accelerator system. The principal components are discussed in the order of where the system starts.

Injector Configurations

The injector configuration consists of the ion source and injector magnets. This is the stage where the ion beam is created and thereafter injected into the accelerator tank. There are various types of ion sources available to create desired ions. At CMAM, there are two ion sources available which can create ions for any element ranging from H to U. These sources are the Duoplasmatron and the sputtering ion source. For this research study, the Duoplasmatron source was used and will therefore be discussed in more detail below.

Duoplasmatron Ion Source

The HVEE Model 358 Duoplasmatron ion source is manufactured by High Voltage Engineering Europa (HVEE) which is a gas source that is mainly used to produce H and He ions. Some of its key features include high currents from gaseous elements, positive and negative ions, reliable operation, low energy spread, high brightness, a filament life greater than 1000 hours and easily replaceable components. It was designed in such a way that high vacuum techniques can be utilized in order to minimize contamination and contribute to efficient operation and pure ion beam outputs.

The source is a modified Van Ardenne ion source and is a useful plasma source for extracting positive and negative ions. In the source, there is a two-stage discharge involved in generating the ion beam. The first discharge is sustained by thermionic electron emission from a filament (cathode). An intermediate electrode acts as the anode for the first discharge and is equipped with an aperture in its centre. The discharge is guided through the axial magnetic field in the aperture into the second discharge chamber. The second discharge is maintained between the intermediate electrode, which now acts as a cathode, and the main anode. The strong axial magnetic field generated in this region confines the plasma in a small volume, and is responsible for the high plasma density. The ions from the second discharge flow through the anode aperture into the extraction region [51].

5 MV Accelerator Tank

The 5 MV tandem accelerator is an extended voltage range of the 3 MV tandem accelerator. The 5 MV tandem was deigned to fulfil demands of higher terminal voltages to perform heavy element ERDA and NRA, positron emission tomography (PET), deep-level light-ion implants in semiconductors and accelerator mass spectrometry. The new design is based on an all-solid-state parallel-fed Cockroft-Walton power supply which is constructed around a high-energy tube. With the introduction of the coaxial design of the power supply around the high-energy accelerator tube, the characteristic T-shaped tank of the High Energy Voltage (HVE) has been changed to a beam-line accelerator. In the T-shape design, the power supply stack is placed perpendicular to the accelerator tubes and due to the required size

and mechanical stability of the system it would be impractical for the $5MV$ system to have the same design. An image of the accelerator tank found at CMAM is shown in Figure 4.3.

The accelerator tank supports the following components that all contribute to supplying ions:

- **Accelerator Tube**
  At the entrance of the accelerator tube, there is a Q-snout electrode. A certain voltage applied to this electrode which allows it to act as a focussing lens to the accelerator. Inside the accelerator tube is a tapered pressure tank that contains 8 bars of SF_6 which act as an insulating medium. The tank has a diameter of $2.6m$ at the terminal and an overall length of $8.7m$. The accelerator section of the tank consists of two low-energy tubes, a stripper canal and two high-energy tubes. These large diameter acceleration tubes are designed in such a way that they optimise high pumping speeds. There are dividing resistors mounted on the perimeter of the tube electrodes that distribute the voltage along the tubes homogenously.

Figure 4.4: Accelerator tank at CMAM.

- **Stripper canal** The stripper canal has a turbo-molecular pump that re-circulates the stripper gas. After the incoming negative ions have entered the stripper canal, one or more electrons are stripped from the ions and all that remains are positive ions. The canal is located in a terminal that is fed with argon gas. The gas is pumped away from between the stripper canal and the accelerator tubes on either side and is subsequently re-circulated by the turbo-molecular pump.

- **Coaxial power supply**
  The voltage generation in the new Tandetron system is based on the all-solid-state Cockroft-Walton power supply. Cockroft and Walton

used a high voltage generator with multiple rectifier stages that is capacitively coupled to a source of alternating current (AC) power. The generator and rectifying stages are configured in a series-coupled system. In this type of system, the lower stages in a cascaded rectifier circuit transmits AC to the upper stages. The transmitted AC reduces the direct current (DC) generated under the load in the upper stages [52].

A solid-state radio-frequency (RF) driver supplies power to an oscillator circuit that consists of a transformer coil and two dynodes. The transformer tank is mounted sideways on the main tank, close to the high-energy base plate. The two dynodes serve the purpose of capacitively coupling the electrical power to the diode stacks via the corona rings. The fraction F_{coup} of the dynode voltage V_{DYN} that is present on the corona rings is expressed by:

$$F_{coup} = C_{DC}/2C_{CC} + C_{DC} \tag{4.10}$$

where C_{DC} is the capacitance of the dynode to corona ring and C_{CC} is the capacitance between the two opposing corona rings. The diode stacks are mounted between opposing corona rings and rectify the RF voltage on the corona rings to generate the DC terminal voltage (U_{TV}) and can be expressed by:

$$U_{TV} = 4nF_{coup}V_{DYN} \tag{4.11}$$

where n is the number of corona rings [53] [9].

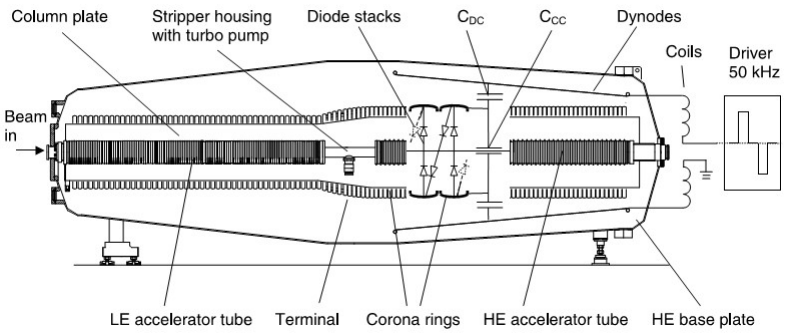

Figure 4.5: Layout of the 5 MV tandetron [9].

- **Bending/Analysing Magnet**
  Right after the accelerator tank, there is a bending/analysing magnet. This magnet is used to help control the terminal voltage of the accelerator and restrict the beam exiting the accelerator tank. It is well

known that charged particles that enter a transverse uniform magnetic field will be forced to follow a circular path, the radius of which depends upon the ratio of the particle's momentum to its charge (P/Q). A dipole magnet whose field is generated by current carrying coils above and below the beam line is used. By controlling the current in the magnet, the magnetic field can be controlled, which in turn fixes the radius of curvature of the particles entering the field. The magnetic field can be set such that only the beam of interest will travel along a path that will allow it to exit the magnet. All the other beams entering the magnet collide with the walls of the vacuum box and never reach the target. When the voltage is set to an exact value, the particles have precisely the right energy and are bent by the magnet so that they pass through the slits.

To control the terminal voltage of the accelerator, a set of metal slits are placed near the exit of the analysing magnet, with the opening between the slits centred on the exit of the magnet. If the terminal voltage drops slightly, then the particles entering the magnet have less than the desired energy, and are bent a bit too much by the magnetic field. These particles strike the slit on the right or left side. The difference in the amount of beam current hitting the beam on the right and left sides is then an indication of whether the beam energy is too high, too low, or just exact, the signal is therefore fed back to the stabilizer and used to control the corona tube grid bias.

4.1.3 Magentic Force Microscopy

The magnetic force microscopy hereafter referred to as the MFM, is a secondary imaging mode of the atomic force microscopy technique (AFM). It is derived from the tapping mode of the AFM with the tip coated with a thin ferromagnetic film as compared to the AFM that uses a normal non-magnetized tip. The MFM is a technique that maps the magnetostatic forces present across the surface of a sample. Attractive or repulsive forces act between the tip and the sample which then creates an image of the spatial variation of the magnetic field. The MFM detects the changes in the resonant frequency of the cantilever that is induced by the magnetic interaction with the sample surface. The interaction between the tip and the sample can also be probed using the scanning tunnelling microscope (STM) and has been reported in literature by a number of researchers including Allenspach and Bischof [54], Moreland and Rice [55], to name few. The images obtained by the MFM are a result of the convolution of the magnetic properties of both the sample and the probing tip.

To describe the force and interaction energy of a system consisting of a

probing tip and a sample, integrations across the volume and surface have to be performed using the following equations:

$$F = (\mu \times \nabla) \times B = (\mu \cdot \nabla)B = \nabla(\mu \cdot B) \tag{4.12}$$

and

$$W = -\mu \cdot B \tag{4.13}$$

where F is the force, m is the total magnetic dipole moment, B is the external magnetic induction and W is the interaction energy [56]. The basic theory of magnetostatics is discussed in detail in in a book by S. Dror [56] where the interaction between two magnetized media is discussed in full detail. The MFM operates in a dual scanning lifted mode. The Lift-mode measures both the topography of the sample and another property like the magnetic force (MFM) or the electric force (EFM), one scan after the other. The information captured from the topographical scan is used to track the probe tip at a constant height above the surface of the sample during the second scan. Since the magnetic forces interact at much greater distance than the weak van der Waals forces, the electrical or magnetic force information received during the scans can be separated from the surface topography by easily increasing the tip-to-sample distance by lifting the tip up, i.e. lifted mode. This is better illustrated in the Figure below.

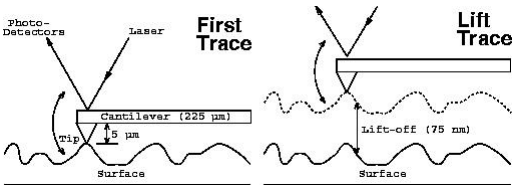

Figure 4.6: Dual Scanning showing the First Trace and the Lift Trace.

During the dual scanning process, the tip first acquires the surface topography in tapping mode. The tip is then lifted up and is retraced onto the surface profile while maintaining a constant height between the tip and surface of the sample. For the second scan, the tip is no longer driven by the piezo-actuator since there is no feedback required. As the tip moves over a magnetic field gradient, it is either attracted or repelled by the sample depending on the direction of the magnetic moment of the sample. This is illustrated in the Figure below. The deflection of the cantilever is proportional to the magnetic field strength and can be measured using the standard light-lever system.

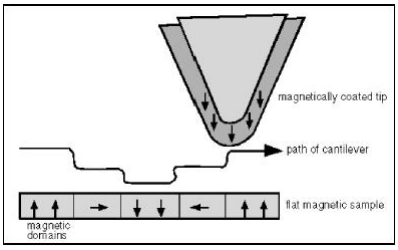

Figure 4.7: Magnetic tip moving along the surface of a magnetic sample.

4.1.4 Monte Carlo Simulations

Monte Carlo simulations are a method used to quantitatively describe the energy loss of ion-solid interactions. A detailed review on ion-solid interactions computer simulstions is discussed in a book by Eckstein [57]. The Monte Carlo method is the most common computer program used to simulate the slowing down and scattering of energetic ions in amorphous targets. Biersack and Haggmark [58] give a detailed explanation of the ion-solid interactions. The program is used to determine the ion range and damage distributions of ions as well as the angular and energy distribution of transmitted ions. The program has high efficiency and accuracy which is achieved through the application of an analytical formula that determines the nuclear scattering angles and also expands the distance between collisions at high energies. The program is used to calculate the range distributions of a variety of ion/target combinations [59].

Monte Carlo simulations can be performed using the Stopping Range of Ions in Matter (SRIM) software package. The software is a compilation of various programs including the Monte Carlo program that calculate the stopping and range of ions with energies 10 eV-2 GeV/amu into matter using a quantum mechanical treatment of ion-atom collisions. An "ion" in this case refers to a moving atom and "atom" is any target the ion interacts with. What happens during the ion-atom collisions is that the ion and atom have a screened Coulomb collision combined with the exchange and correlation interactions which can be found between the overlapping electron shells. Within the target, plasmons and electron excitations are created from the long range interactions between the ion and target atoms. The calculation is setup in such a way that it describes the ion-atom interactions by including a description of the targets collective electronic structure and interatomic bond structure [58].

Transport of Ions in Matter (TRIM) is a program found within the SRIM software package and is the most comprehensive. This is a Monte-Carlo calculation that follows the transport of the ion into the target, it makes a

detailed calculation of how the energy is transferred to every target atom during the collision. The program will accept/simulate energy transfer of ions into complex targets that are made of compound materials of up to 8 layers, each layer being a different material. It calculates both the final 3-dimensional ion distribution and also all the kinetic phenomena that are associated with the ions energy loss. These phenomena include target damage, sputtering, ionization and phonon production. The target atom cascades are followed in great detail. The program is designed in such a way that it allows one to pause your calculation and resume later. Statistical algorithms are used to perform very efficient calculations such that an ion can make jumps between calculated collisions and it then averages the collision results over the intervening gap.

4.1.5 Raman Spectroscopy

Raman spectroscopy is the study of the change of frequency when light is scattered by molecules. A Raman spectrum is a set of Raman frequencies of the scattering species constitutes. The Raman frequency is determined by measuring the frequency shift. If we consider the frequency of the incident light to be v_0 and the frequency of the scattered light to be v, then the frequency shift is given by: $v_0 - v = \triangle v$. The frequency shift can be positive or negative and its magnitude gives us the Raman frequency of molecule [60].

Raman spectroscopy occurs between two photons where there is a change in polarizability of a molecule with respect to its vibrational mode. An induced dipole moment is created within the molecule when the polarizability of the molecule interacts with the incoming radiation that comes in the form of light. The induced moment emits radiation that contains Raman scattering. The scattered light consists of two different types of scattering, namely the Rayleigh scattering and the Raman scattering. When the scattered light has the same frequency as the incident light then we say that the light has undergone Rayleigh scattering. In Raman scattering, there is a shift in the frequency of the emitted light from the frequency of the incident radiation by the vibrational energy that is gained or lost.

The polarizability can be expressed with a tensor that contains two cartesian components. The first component is associated with the incident photon while the other is associated with the scattered photon. The two photons are connected in a single quantum mechanical process and can be expressed as:

$$\overrightarrow{\alpha_{\alpha\beta}} = \frac{1}{\hbar} \sum_{j \neq m,n} \left(\frac{\langle m|\hat{\mu_\alpha}|j\rangle\langle j|\hat{\mu_{beta}}|n\rangle}{\omega_{jn} - \omega_0 + i\Gamma_j} + \frac{\langle m|\hat{\mu_\beta}|j\rangle\langle j|\hat{\mu_\alpha}|n\rangle}{\omega_{jm} - \omega_0 + i\Gamma_j} \right) \tag{4.14}$$

where $\hbar$ is Planck's constant divided by 2π, the summation is over all excited electronic states of j of the molecule, n and m are states that are distinguished by the vibrational quantum energy, $\omega_{jn/m}$ is the angular frequency difference between the states j and n/m; and the terms $i\Gamma_j$ are imaginary terms that are proportional to the vibronic state j [10].

The energy level diagram illustrates IR absorption and Raman scattering, we notice that in both cases the initial state is at the zeroth vibrational energy level of the ground electronic state. Unlike IR absorption where the first vibrational level of the ground electronic state is reached in one step, the Raman scattering requires two steps to achieve this energy level. The energy level diagram shows the vibrational transition from g_0 to g_1, we observe that the scattering photon eergy $\hbar\omega$ is shifted from the incident laser radiation energy by the IR vibrational energy $\hbar\omega_v$ gained by the molecule.

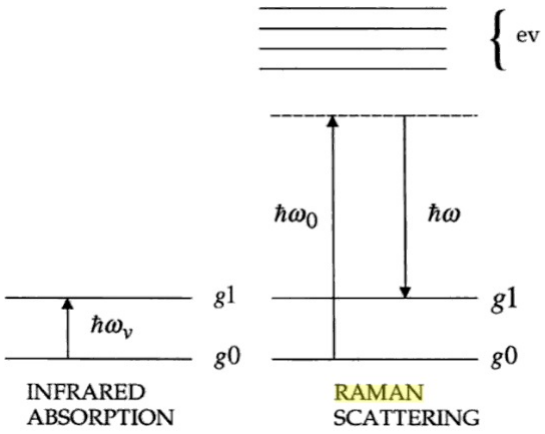

Figure 4.8: Energy level diagram for IR absorption and Stokes Raman scattering [10].

The photon energy of the Raman are well above that of the IR photon or energy of the vibrational transition. The excited vibronic states of the molecule are indicated in the energy level diagram as ev for the v^{th} vibrational level of the e^{th} electronic state. When the molecule gains vibrational energy then we refer to the scattering as Stokes Raman scattering and when the molecule loses vibrational energy then we refer to the scattering as anti-Stokes Raman scattering [10].

4.2 Methodology

Ultra-pure type IIa diamond sample with dimensions $4mm \times 4mm \times 250\mu m$ was used in the experiments performed. The sample was purchased from

Element Six, De Beers South Africa. To start the experiments, calculations of the number of vacancies produced by the proton irradiations on pure diamond were done. As already mentioned, Monte Carlo simulations were performed using SRIM. The results obtained from the simulations will be tabulated and shown in the results and discussion section to follow. Before the irradiation was done, pre-irradiation measurements using the MPMS XL (5T) system were performed on the diamond sample at CSIC. The sample was mounted onto one of the standard sample holders (sample holder number 5) whiich was specially designed for the SQUID as shown in the image below. This sample holder has been used in previous experiments involving diamond and graphite. The sample was fixed onto the standard sample holder using diluted GE 7031 varnish.

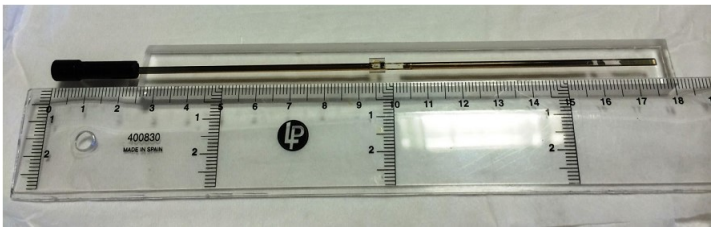

Figure 4.9: Sample holder with diamond sample attached to it.

The sample holder was then attached to the SQUID sample rod that goes inside the sample chamber of the MPMS (5T) system. The sample rod can be seen in the image below, with the sample holder attached on the far end of the rod.

Figure 4.10: Sample rod for the SQUID.

Once the sample was attached onto the SQUID sample rod, it was inserted into the chamber. The computer operating system was then programmed to sweep through a field of 50 kOe at temperatures 4.2 K and 300 K. It was also programmed to measure the temperature dependence in the temperature range of 2 K to 300 K at a fixed field of 2 kOe. Subsequently, the sample was detached from the sample holder and cleaned using ethanol under ultrasound at CMAM where the irradiations would take place. Once

again, varnish was used to fix the diamond sample onto a copper substrate with a hollow centre.

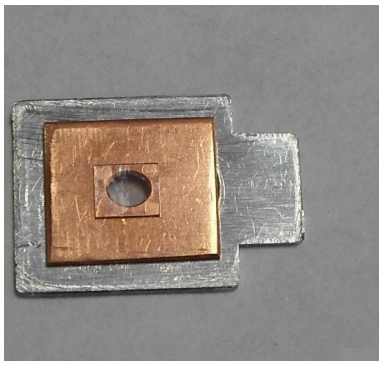

Figure 4.11: Diamond sample fixed on copper substrate and aluminium sample holder.

The copper substrate was then fixed onto the sample holder of the internal microbeam line. A copper substrate was used to hold the sample since the hollow centre of the aluminium sample holder was too large for the sample to be attached directly to it. The sample holder was then attached to the sample rod of the internal microbeam line.

Figure 4.12: Sample holder being attached to the microbeam line sample rod.

After the sample holder was attached onto the sample rod, the sample was inserted into the sample vacuum chamber at the end of the internal microbeam line for irradiation. The sample chamber is kept in vacuum to avoid contamination of the sample and to avoid interactions of the protons with cosmic rays and other particles that may be found in free space. The sample chamber has a viewport from which one can see the sample inside the chamber.

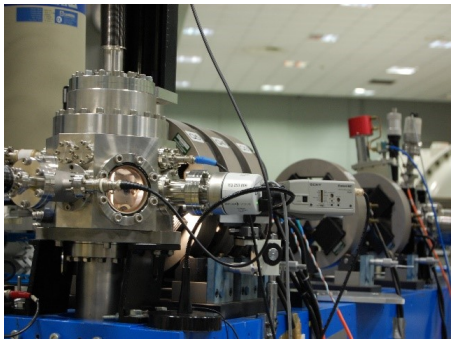

Figure 4.13: Sample vacuum chamber.

The position of the sample is adjusted manually and can be seen in the image below where one of our collaborators was adjusting the position of the sample.

Figure 4.14: Diamond sample being positioned to be in line with the microbeam.

Thereafter, the sample was placed inside the vacuum chamber and was fixed in line with the microbeam line. The whole system was controlled remotely from the control room to avoid radiation exposure. A software was used to control the beam to scan according to the desired pattern of the irradiation, the sample was scanned following ideally $1 \times 1 \mu m^2$ pixels until the corresponding dose was implanted. This scan went in a circular fashion from outside to inside the figure. An image of the control room is shown in the image below, the multiple screens show the various components of the tandem accelerator and its surroundings.

Figure 4.15: Control room.

Post irradiation; the sample was detached from the microbeam line sample holder, cleaned with propanol under ultrasound and fixed onto the sample holder for the SQUID using the same diluted GE 7031 varnish as before. The sample was carefully placed in more or less the same position as in the pre-irradiation measurements. The sample was taken back to CSIC where the SQUID measurements were performed again under the same conditions as the pre-irradiation measurements. Raman spectroscopy measurements were performed to observe the structural damage induced by the irradiation. Futhermore, AFM and MFM measurements were performed to measure the topography and the magnetic signal over the irradiated regions.

4.2.1 Irradiation Details

As mentioned previously, irradiations were done over a period of three days. The sample was irradiated with proton energy of $2.2MeV$ and a fluence of 5.0×10^{17} ions/cm^2. 29 stripes were irradiated on the diamond sample over a period of 3 days. Each stripe was $1.2mm$ long with several different widths and spacing between them, the width and spacing of the stripes is discussed in detail below. The total implanted dose was determined to be $503\mu C$ with a total irradiated area of $0.63mm^2$. The proton current varied in the range of $6 - 8nA$ and the beam spot area was $\approx 10\mu m^2$.

Following the chronological order of the irradiation, seven sets of stripes (A-G) were made in three consecutive days. Every set comprises of either 4 or 5 stripes except for set D, which only has a single stripe. All the stripes have dimensions $1200 \times 20\mu m^2$ except for those marked by $*$. The first set of stripes (A) have a spacing of $20\mu m$ between them but in practice, this spacing is much less due to the lateral resolution or halo of the beam. The rest of the sets have a spacing of $40\mu m$ between each stripe.

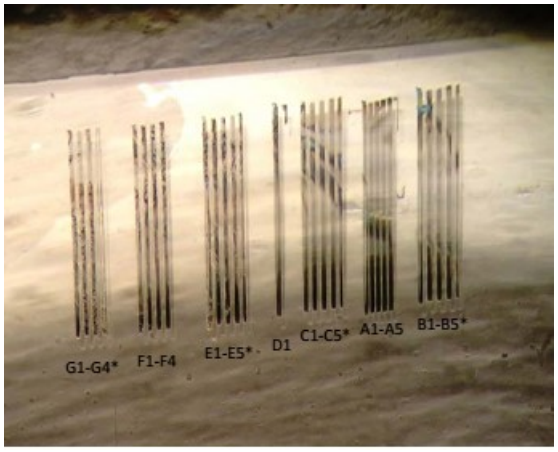

Figure 4.16: Diamond sample with irradiated stripes.

Focusing on the stripes marked by $*$, which can be seen in the image below:

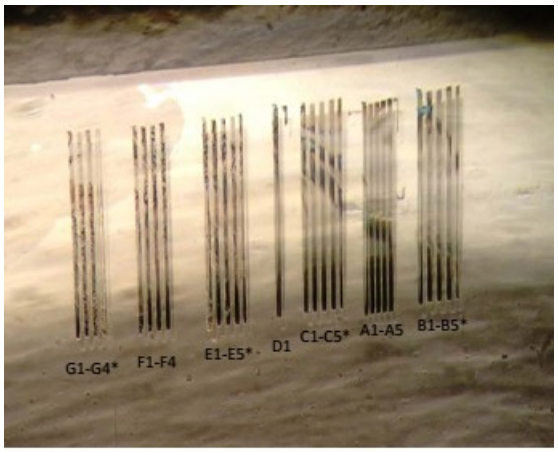

Figure 4.17: Enlarged image of diamond sample with irradiated stripes.

- B5: This should have been a $10\mu m$ width stripe, but only the most left and most right vertical lines were irradiated which resulted in a $1\mu m$ wide stripe on either sides,
- C5 and E5: These are $10\mu m$ width stripes (half a typical line from the other lines),
- G4: This should have been a $20\mu m$ width stripe, but only the two most left and two most right lines were irradiated thus resulting in $2\mu m$ wide lines on either sides.

The image below shows the sample after irradiation; if we look carefully at the sample, we can see the stripes made by the microbeam. These are positioned on the top of the diamond sample (5 black stripes on the diamond).

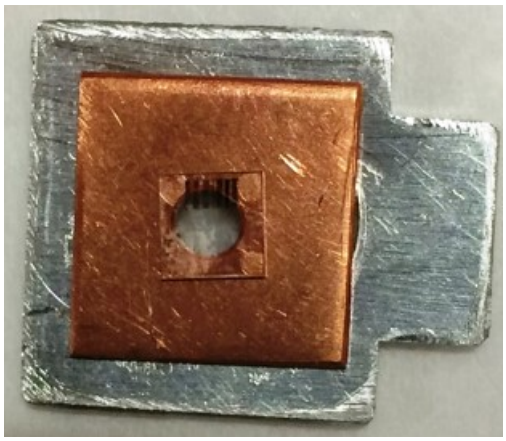

Figure 4.18: Diamond sample after irradiation

Chapter 5

Results and Discussion

5.1 SQUID Analysis

Pre-irradiation measurements were performed on the sample. Using the MPMS system, the magnetic moment measurements were taken by systematically sweeping the field from 0 to 50 kOe with fairly small steps at two temperatures (4.2 and 300 K). Thermal cycle measurements from 4.2 to 300 K with fairly small steps at a constant field (2 kOe) were also obtained. The pristine sample exhibited an almost perfect diamagnetic signal which is independent of temperature as expected. Figures 5.1 and 5.2 below show the magnetization curves of the sample. Figure 5.1 shows the field dependence graph at constant temperatures 4.2 K and 300 K and figure 5.2 shows the temperature dependence magnetization curve at constant field, 2 kOe. On the curve it is observed that the magnetization is independent of temperature, it shown by the coincidence of the data points at temperatures 4.2 and 300 K. The curve shows a strong dominant diamagnetic signal of -1.9×10^{-8} emu/Oe, which is the slope of the curve. Taking into consideration the mass of the sample which was 14.04 g, the diamagnetic susceptibility for the diamond sample is -4.75×10^{-7} emu/g.

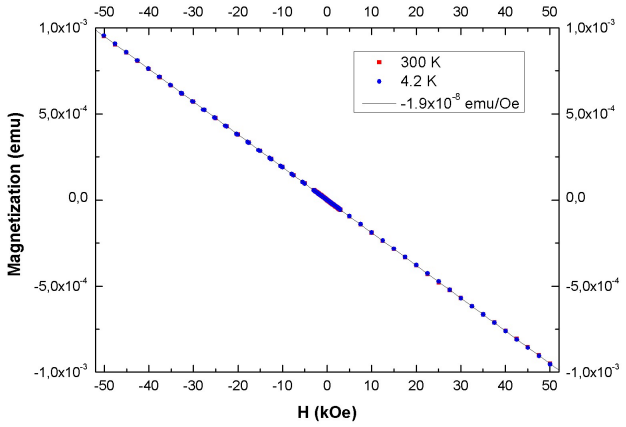

Figure 5.1: Field dependence of the magnetic moment of diamond at temperature 4.2 and 300K before irradiation

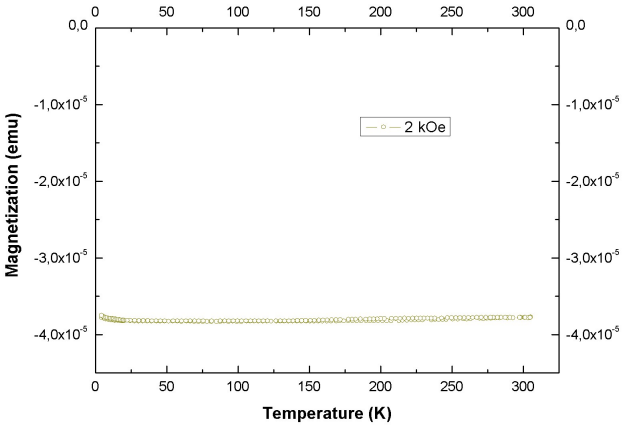

Figure 5.2: Thermal cycle at constant field 2 kOe before irradiation.

The diamagnetic susceptibility of the sample (-4.75×10^{-7} emu/g) is in agreement with that reported in the literature (-4.9×10^{-7} emu/g) [12]. The figure below is extracted from Heremans et al. and shows the behaviour of temperature dependent moments of various carbon structures, the behaviour observed above is similar to that reported in the literature [1].

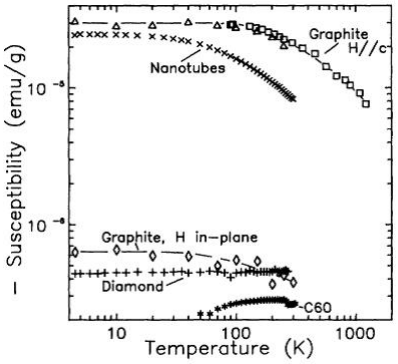

Figure 5.3: Summary of the temperature dependence of the susceptibility of the various carbon structures [1].

After the dominant diamagnetic signal of $(-1.9\times10^{-8}\ emu/Oe)$ has been subtracted from the data, a very weak magnetic contribution is observed at 4.2 K as shown in figure 5.4, however does not occur at room temperature (300 K). The origin of this weak magnetic contribution is unknown since it only appears at very low temperatures. The signal can either be result of possible impurities found within the sample or from the varnish. The varnish used (GE 7031) however is specifically designed to be used in the SQUID magnetometry and is recommended by Quantum Design manufacturers of the MPMS system, therefore it can be disregarded that the varnish contributed to any signals observed [61].
Figure 5.4 shows the field dependence of the magnetic moments after the dominant diamagnetic signal had been subtracted. The hysteresis loop at 4.2 K follows an s-like curve after the subtraction of the dominant diamagnetic signal.

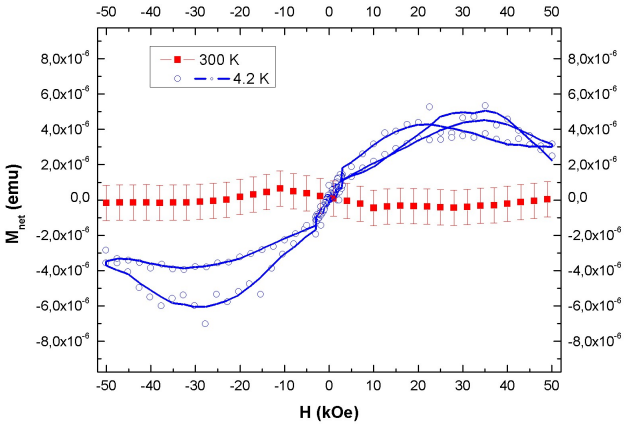

Figure 5.4: Field dependence magnetic moment with dominant diamagnetic signal excluded.

The sample was irradiated with proton fluence 5.0×10^{17} $ions/cm^2$. After irradiation, magnetization curves at 300 K and 4.2 K and the thermal cycle at a fixed magnetic field of 2 kOe were obtained. Both graphs exhibit similar diamagnetic behaviour to that before irradiation but a small and positive magnetic contribution was observed. The positive magnetic contribution is better observed on the thermal cycle curve where it is clearly shown that the magnetization of the sample increased which can be seen on the curve on figure 5.5. Figure 5.6 shows the field dependence of the magnetic moments at the same temperatures as those that were taken before irradiation. Focusing closely on the data points, it is seen that they have moved slightly below and above the dominant diamagnetic signal (-1.9×10^{-8} emu/Oe) that was observed in the pristine measurements. This clearly indicates that the irradiation has made some changes within the structure of the diamond.

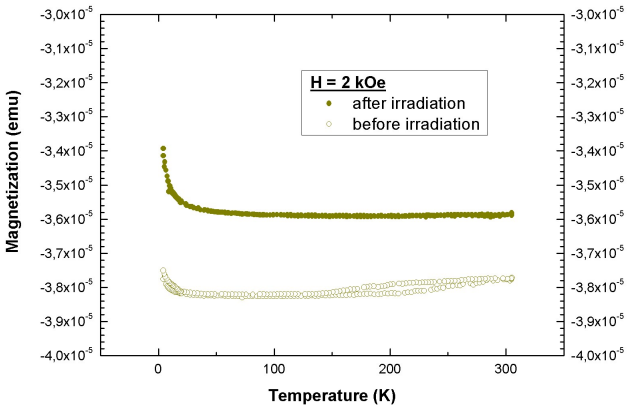

Figure 5.5: Thermal cycle at constant field 2 kOe after irradiation.

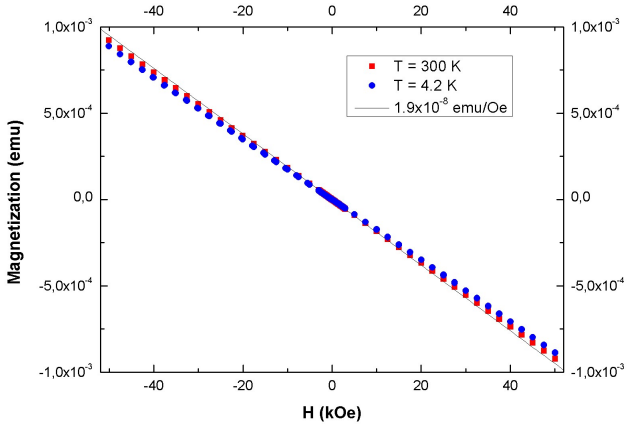

Figure 5.6: Field dependence of the magnetic moment of diamond at temperature 4.2 and 300 K after irradiation.

To determine the net magnetization (M_{net}), the diamagnetic backgrounds from the pristine sample were subtracted from the irradiated measurements. The dominant linear background of -1.9×10^{-8} emu/Oe was eliminated from the field dependence magnetization curve. The net difference of the thermal cycles taken at 2 kOe was determined by either excluding the constant value of -3.8×10^{-8} emu which was obtained from the pristine sample measurements, this can be seen in figure 5.5. Another way was to subtract the curve obtained before irradiation from the curve obtained after irradiation, this curve is represented with the purple data points on figure 5.8. Figure 5.7 shows that the main outcome of the irradiation is a param-

agnetic contribution. Additional superparamagnetic and ferromagnetic-like contributions were also observed and cannot be overlooked. The signal observed is almost temperature-dependent at temperatures below 50 K and then becomes temperature-independent at temperatures above 50 K. A temperature-independent difference of $\sim 2 \times 10^{-6}$ emu is observed as shown in figure 5.8.

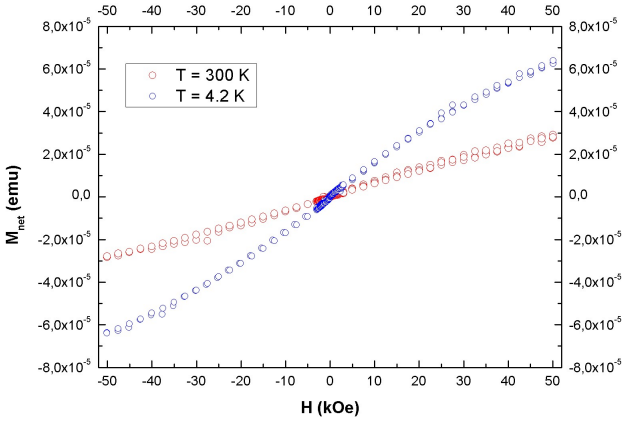

Figure 5.7: Field dependence of the net magnetization of diamond at temperature 4.2 and 300 K after irradiation.

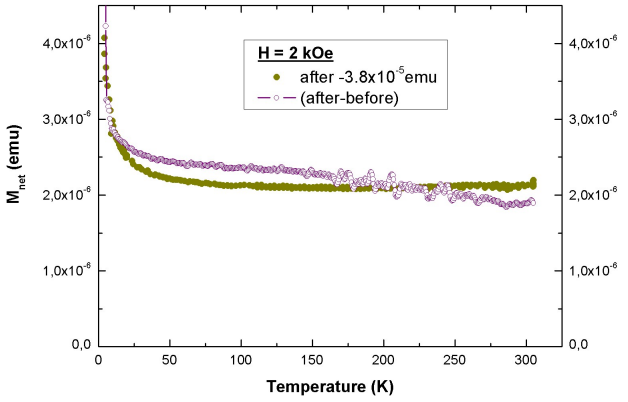

Figure 5.8: Net difference thermal cycles at constant field 2 kOe after irradiation.

Figure 5.7 and 5.8 indicate that the main outcome from the irradiation is a paramagnetic contribution, but there are additional superparamagnetic

or ferromagnetic-like contributions that cannot be disregarded. These additional contributions observed are unclear to what their origin is and could be the varnish employed during the experimental procedures or it could be due to the fact that the irradiation may have caused damage in the structure of the diamond. The damage could have caused some of the electrons to be unpaired and hence induced a ferromagnetic-like signal. It makes no sense to suggest that the varnish is responsible for the additional contribution since the varnish was not exposed to the microbeam of protons during irradiation, and so we can conclude that the changes are a result of the structural damage of the diamond sample.

The damage induced by the irradiation can be clearly observed in the graphs below. The net magnetization before and after irradiation are compared both at room temperature (300 K) and lower temperature (4.2 K) respectively. A change in the long magnetic moment is clearly observed.

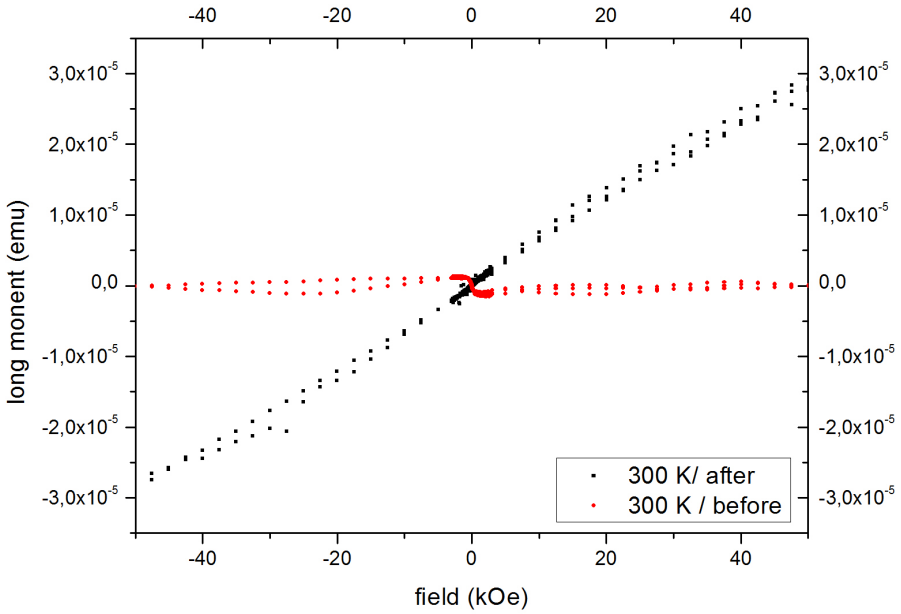

Figure 5.9: Net magnetization before and after irradiation at 300 K.

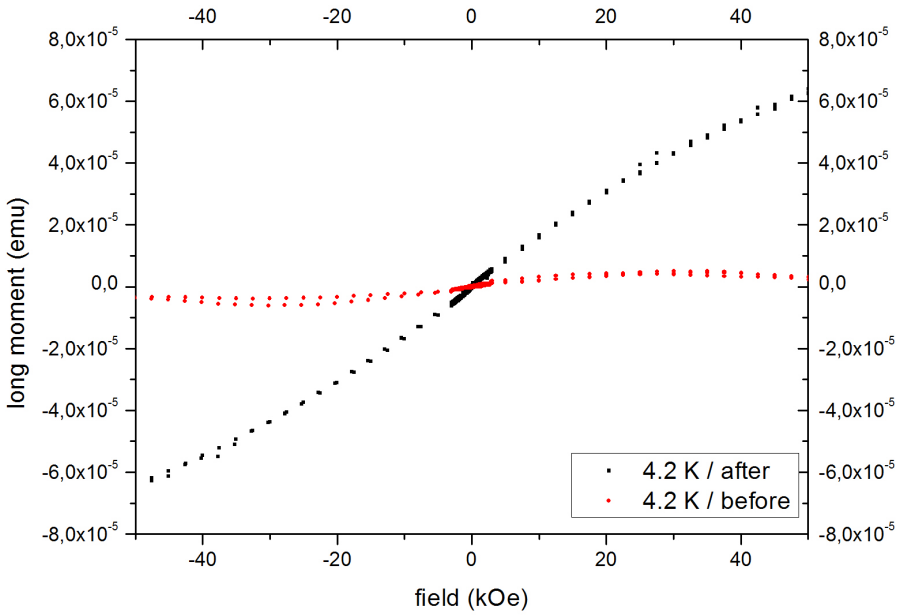

Figure 5.10: Net magnetization before and after at 4.2 K.

To further investigate the net magnetization of the sample after irradiation, the central low-field zone was amplified to investigate ferromagnetic (FM) coercive field in the low temperature curves. The FM coercive field is the intensity of an applied magnetic field required to reduce the magnetization of that material to zero after the magnetization of the sample has been driven to saturation. It measures the resistance of a ferromagnetic material to become demagnetized. The curve below shows the central low-field zone investigating the possible ferromagnetic (FM) coercive field at low temperatures, unfortunately it is not very clear in the curve. The white data points in figure 5.11 show the data for pre-irradiation and the blue data points show the data for after irradiation.

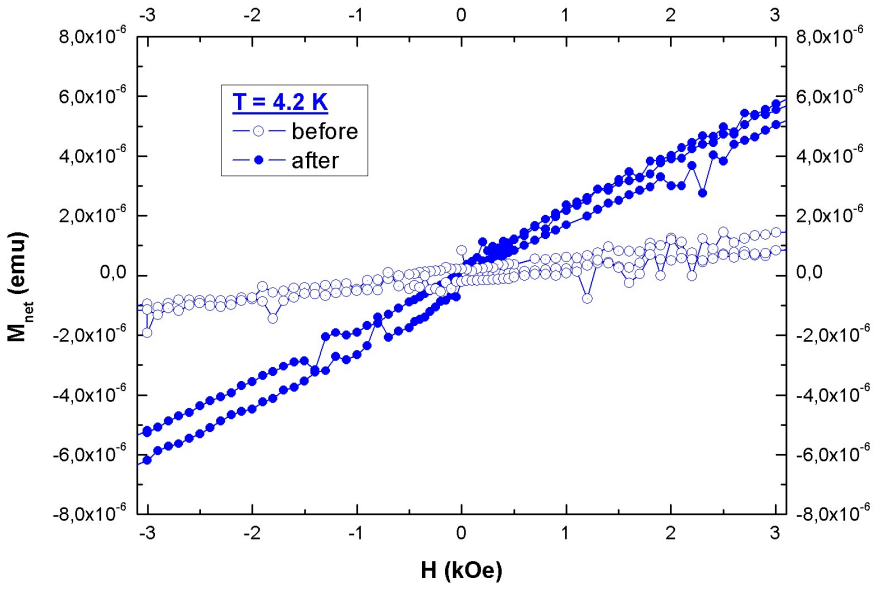

Figure 5.11: Central low-field zone to seek a possible FM coercive field in low temperature curves.

The Curie law for paramagnetism is fitted onto the net paramagnetic signal after irradiation therefore allowing for a constant term to account for any additional diamagnetic or ferromagnetic contribution. The expression for the Curie law is given by:

$$M_{net} = C/T + b \tag{5.1}$$

where C is the Curie constant, T is the temperature, M_{net} is the net magnetization and b is the constant term.

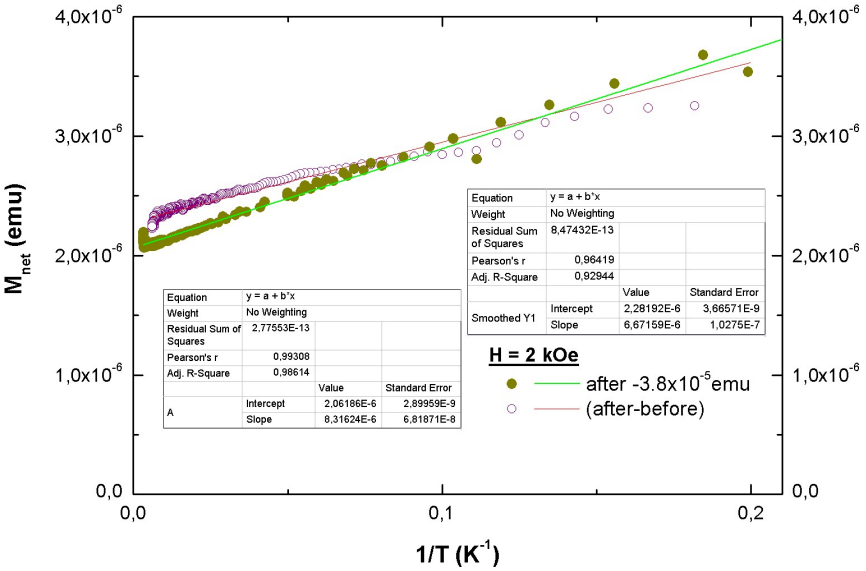

Figure 5.12: Curie Law fit onto the net paramagnetic signal.

Looking at the results of the Curie Law fit, we obtained that:

$$C = 6.7 - 8.3 \times 10^{-6} emu \cdot K \tag{5.2}$$

Taking the average of the 2 curves, the Curie constant is given by:

$$C = 7.5 \times 10^{-6} emu \cdot K \tag{5.3}$$

The constant term b is given by:

$$b = 2.1 - 2.3 \times 10^{-6} emu \cdot K \tag{5.4}$$

This is the same value that was obtained in figure 5.8 (Net difference thermal cycles at constant field $2kOe$ after irradiation) which shows that the temperature-independent difference is $\sim 2 \times 10^{-6} emu$.
Using SRIM to calculate the relevant parameters, the following information was presented in Tables 5.1 and 5.2.

Table 5.1: SRIM calculations of relevant parameters.

Proton Energy (MeV)	22
Ion Range (μm)	28.5
Longitudinal Straggle (μm)	0.55
Vacancies / ion	11.1
P (vac/ion $\cdot(\mu m)$ at peak ($28.4\mu m$)	4.2
FWHM at Peak (μm)	1.1
M (vac/ion $\cdot(\mu m$ in the middle (Ion range/2)	0.15
S (vac/ion $\cdot(\mu m)$ at the surface ($0 - 1\mu m$)	0.08

Comparing the observed paramagnetism to that of broad beam irradiations previously done on ultra-pure diamond we can see the similarities in the table below:

Table 5.2: Comparison of paramagnetism between broad-beam and microbeam irradiations.

	Broad-beam Sample J1	Broad-beam Sample J2	Microb-beam
Total irradiated area (mm^2)	12.1	14.1	0.63
Total current density ($nA/\mu m^2$)	3.3×10^{-5}	2.1×10^{-5}	0.7
Fluence (ions/cm^2)	3.8×10^{17}	1.0×10^{18}	5.0×10^{17}
Total charge $Q_{total}(\mu C)$	7350	23 600	503
Total number of vacancies (N_{vac})	5.1×10^{17}	1.6×10^{18}	3.5×10^{16}
Currie coefficient C ($emu \cdot K$)	3.2×10^{-5}	4.8×10^{-5}	7.5×10^{-6}

Looking at the correlation between the produced vacancies and the paramagnetism, we remember that the magnetic susceptibility of a material is given by:

$$\chi = M/H = \mu_0 M/B \tag{5.5}$$

where $\mu_0 = 4\pi \times 10^{-7} T \cdot m/A$. From theory, we also noted that the Curie Law is given by:

$$\chi = n(\mu_0 \mu_{eff}^2)/3k_B T) \equiv C/T \tag{5.6}$$

where $\mu_{eff} = g_j \cdot \mu_B \cdot [J(J+1)]^{1/2} \equiv p \cdot \mu_B$ with the Bohr magneton being $\mu_B = 9.274 \times 10^{-24} A \cdot m^2 (= J/T)$. The total magnetization $M(emu)$

measured by the SQUID is given by:

$$M = M \cdot V = \chi HV = N\mu_{eff}^2/(3k_BT(\mu_0 H) \rightarrow C = N\mu_{eff}^2/(3k_B)B \quad (5.7)$$

N is the calculated total number of vacancies denoted by N_{vac} therefore the Curie constant is given by:

$$C = N_{vac} \cdot p^2 \cdot 2.08 \times 10^{-21} emu \cdot K \quad (5.8)$$

It was found in a graphite case that, $p = g_j\sqrt{J(J+1)} = 0.270.02$ therefore $\mu_{eff} = (0.270.02)\mu_B$. In the diamond case, using the broad-beam instead of the micro-beam, the determined Curie coefficients were plotted as a function of the nominally produced number of vacancies for different samples and an increase of paramagnetic coefficient with increasing number of defects was observed. From the data obtained for sample J1, the estimated values for $p = 0.17$, therefore giving $\mu_{eff} = p \cdot \mu_B = 0.17\ \mu_B$. In the case of micro-beam irradiation, $p = 0.32 \pm 0.02$ and therefore giving $\mu_{eff} = p \cdot \mu_B = (0.32 \pm 0.02)\mu_B$. This value is not far off from the typical expected effective value for the magnetic moment of (0.5 - 1)μ_B.

5.2 Raman Spectroscopy

To characterize the structural damage induced by the protons on the diamond, Raman spectra were recorded over the irradiated and non-irradiated regions. An optical image was taken over one of the irradiated stripes. We focus on the D1 stripe since there is enough un-irradiated areas around it for comparison reasons. The optical image was captured at 60 μm and then further zoomed to 10 μm as seen in the image below. The graphitized area that resulted from the irradiation is observed in the optical image and can also be seen in the AFM topography image. Figure 5.13 shows the optical image is the AFM topography where we can clearly see the graphitized region shown by the lighter shapes in the image.

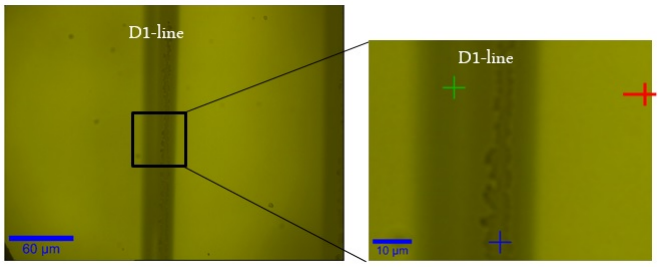

Figure 5.13: Optical image of stripe D1 of the irradiated stripes.

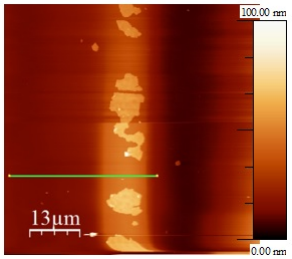

Figure 5.14: AFM topography of the irradiated stripe.

Raman spectra were then measured in three different regions. The first region, indicated by the red cross on the optical image above, is the non-irradiated region of the diamond. The irradiated region that is not graphitized is indicated by the green cross and the third region is the graphitized region that is indicated by the blue cross. As observed in the spectra below, all three regions show an intense line at $\sim 1340\ cm^{-1}$. This line corresponds to the diamond peak but slightly blue-shifted to the reported value in literature ($1332 cm^{-1}$) [28]. Distinctive differences observed from the three regions under study, the most significant difference is observed in the blue spectra that represents the graphitized area.

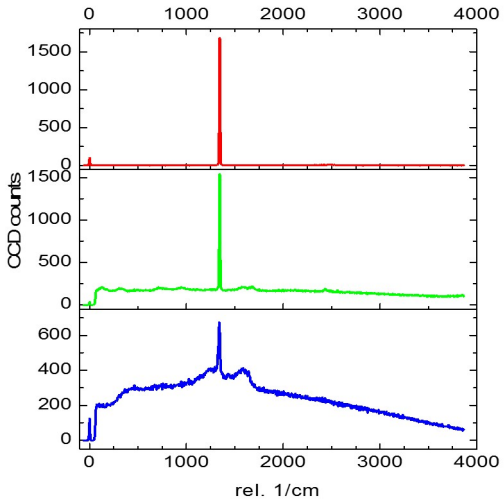

Figure 5.15: Raman spectra of the various regions.

The first difference observed is that there is a red-shift of the diamond peak after irradiation which becomes more distinct when the area is graphitized. This can be observed in the spectrum below were all three spectra of the various regions are plotted into one set of axes to compare the spectra.

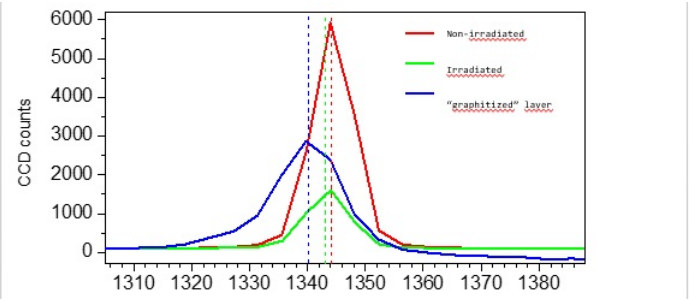

Figure 5.16: Redshift of the diamond line after irradiation.

The second difference is the formation of additional peaks on the irradiated and graphitized regions. To better observe the additional peaks, we disregard the diamond peak and focus more on the other peaks. The bottom and middle spectra from the bottom on figure 5.17 show a formation of an additional peak in the wave number range of 1550 - 1660 cm^{-1} which could be the graphite peak. The additional peaks are highlighted by the yellow(shaded) region in the spectra, we observe two peaks forming in the middle spectrum and a single broader peak in the bottom spectrum. Numerous other peaks are also observed at wave number below 1000 cm^{-1}.

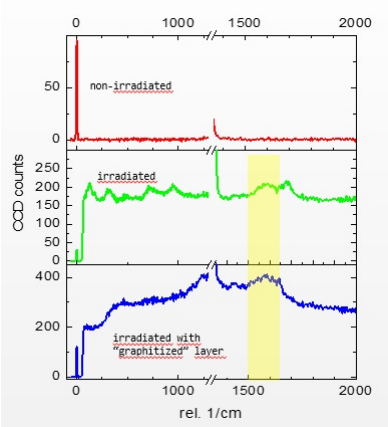

Figure 5.17: Additional peaks observed after irradiation.

Depth analysis was also performed using the confocal Raman that allows measurements of profiles at various depths. Raman spectra were obtained along the marked line in the optical image that comprises of the three regions we have been focusing on, with different values of z from the surface to 10 μm. Below is the optical image with a map that corresponds to the integrated intensity of the diamond line below it. The integrated intensity is marked with a blue box in the Raman spectra below.

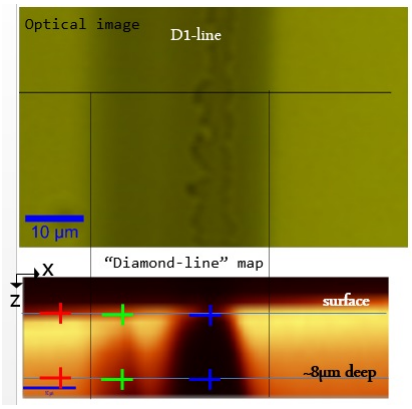

Figure 5.18: Optical image and map of the diamond line.

Comparing the spectra obtained at the surface to those taken deeper into the surface, we notice that no observable signal is detected for the graphitized region. The layer compresses the Raman signal completely, whilst the irradiated and un-irradiated regions show changes that decrease in intensity but the respective features are preserved.

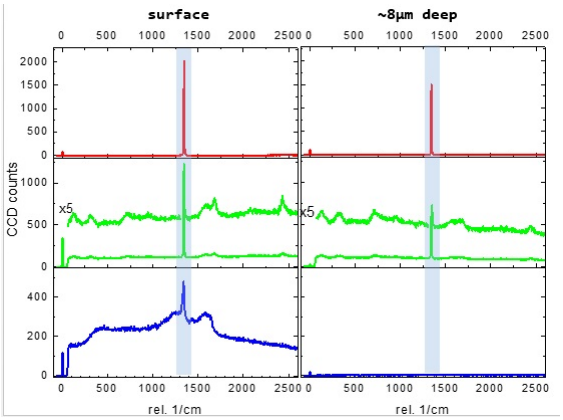

Figure 5.19: Raman spectra of the diamond sample on the surface vs 8 μm.

Integrating the peak around $\sim 1580\ cm^{-1}$ that is indicated by the blue rectangle in the spectra below, we observed a peak that is related to the so-called "G-peak" observed in graphite samples. The second map is observed with the integrated intensity between 580 cm^{-1} and 860 cm^{-1}, indicated by the pink rectangle in the spectra.

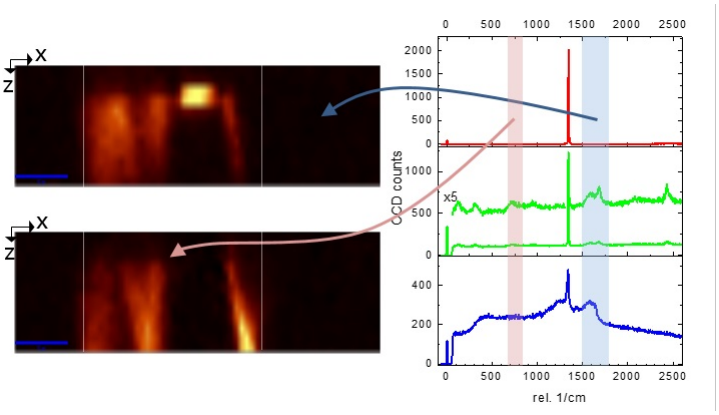

Figure 5.20: Raman spectra of the diamond sample on the surface.

The irradiated area shows different features as compared to those of the un-irradiated area even at $\sim 10\ \mu m$ into the sample. The graphitized layer shows a different Raman spectrum with a wide peak around $\sim 1580\ cm^{-1}$ that can can be corresponded to the graphite. No Raman signal was observed below the graphitized regions.

5.3 AFM and MFM Analysis

From the Raman spectra, we focused on the D1 stripe from the set of stripes that were irradiated on the diamond. We went further and performed MFM measurements over the D1 stripe since the Raman measurements confirmed that the layer observed over the irradiated region is the mixture of $sp2$ and $sp3$ orbitals that caused the surface to graphitize. The graphitized region is shown in the AFM image in figure 5.21 in the topographic and phase signals.

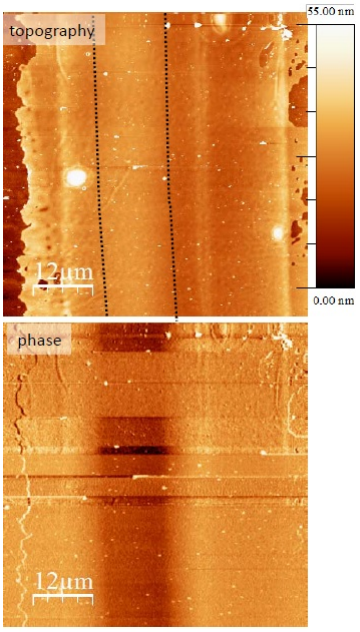

Figure 5.21: Topographic and Phase image of the D1 stripe.

Line profiles over the irradiated regions were measured. From Figure 5.22 and 5.23, we clearly observe the graphitzed regions. The graphitized regions are the lighter "islands" that are observed in the image, with the slightly darker regions showing the irradiated stripe and the dark regions indicating the un-irradiated regions. The line profiles were performed at different scan sizes to better observe the irradiated regions.

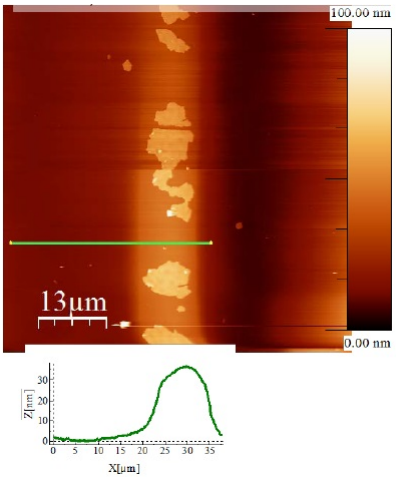

Figure 5.22: Line profile at scan size 13 μm.

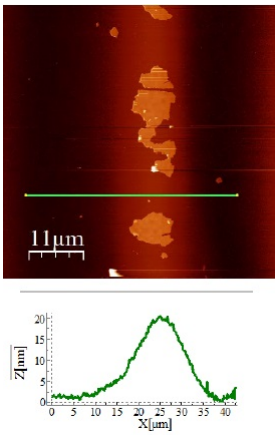

Figure 5.23: Line profile at scan size 11 μm.

Low temperature MFM measurements were performed over the D1 stripe which can be seen in figure 5.24. A magnetic signal is seen in the MFM image with a negative contrast, this is observed by the darker regions relative to the pure diamond corresponding to the graphitic/graphitized region in the topography image. The negative contrast is not completely clear in the MFM image but it can be concluded that there is a change in contrast between the irradiated and un-irradiated regions.

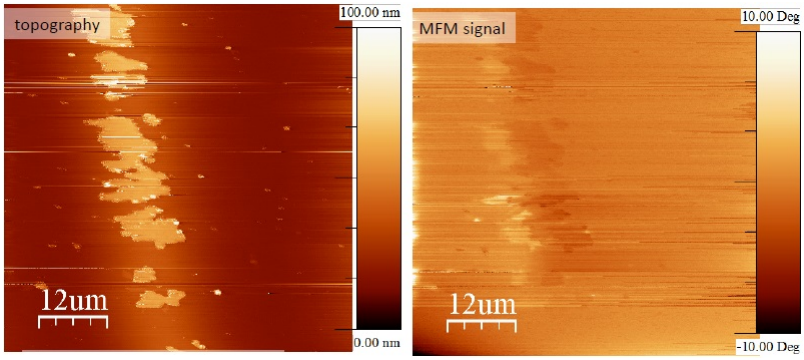

Figure 5.24: Low temperature MFM image.

In figure 5.24, we see the zoomed image of the diamond sample with a part of the irradiated shown. We note that when the field is applied in the positive direction, a weak trough is observed in the MFM image. Whilst when the field is applied in the negative direction, an upswelling/peak is observed over the irradiated region. This effect is better observed in the negative direction as compared to the positive direction. The irradiated region appears to respond to the direction of the applied field at low temperature. This is better observed in figure 5.25.

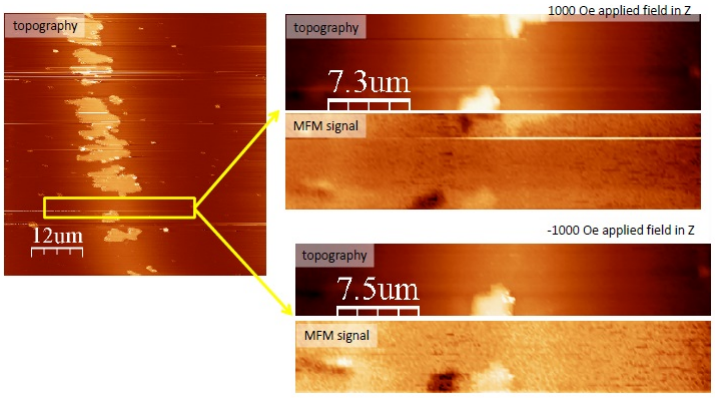

Figure 5.25: Low temperature MFM image.

From the SQUID analysis, Raman measurements and MFM analysis, we can safely conclude that the irradiation resulted in the mixture of $sp2$ and $sp3$ orbitals that graphitized the irradiated surface.

Table 5.3 shows a summary of the results discussed above. The before shows the data of the sample before irradiation and after shows the data of the sample after irradiation. Figure 5.25 is used to illustrate what the different parameters in the table represent.

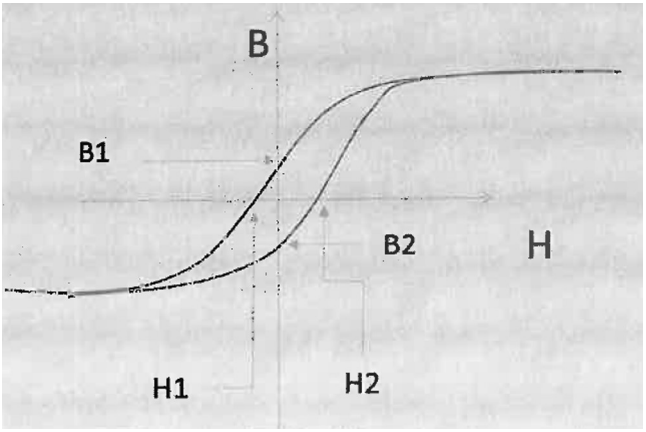

Figure 5.26: Illustration of different parameters shown in Table 5.3.

Sample	Temp	H1	H2	B1	B2	H2-H1
Units	K	Oe ($\times 10^{-7}$)	Oe ($\times 10^{-7}$)	emu	emu	Oe
Before	4.2	-500.6416	600.6788	2.03672	-2.73291	1101.3024
After	4.2	-49.83889	50.029201	1.38709	-1.5646	99.868091
Before	300	N/A	N/A	N/A	N/A	N/A
After	300	-200.000	199.9795	2.01421	-2.19051	399.9795

The Raman shifts can be summarized as:

Area	Diamond Peak	Additional Peak
Units	cm^{10}	cm^{-1}
Non-irradiated	1344	1500 - 1660
Irradiated	1342	1500 - 1660
Graphitized	1340	N/A

Chapter 6

Conclusion

Irradiations were done over a period of three days were the sample was irradiated with proton energy of $2.2MeV$ and a fluence of $5.0 \times 10^{17} ions/cm^2$. 29 stripes in total were irradiated on the diamond sample and each stripe was $1.2mm$ long with several different widths and spacing between them. The total implanted dose was determined to be $503\mu C$ with a total irradiated area of $0.63mm^2$. The proton current varied in the range of $6 - 8nA$ and the beam spot area was $\approx 10\mu m^2$.

The magnetization curves of the pristine (un-irradiated) sample exhibited an almost perfect diamagnetic signal which was independent of temperature. The diamagnetic signal obtained was 4.75×10^7 emu/g and was in agreement with that found in literature [1]. A very weak magnetic contribution was observed at 4.2 K though not at room temperature in the pre-irradiation measurements. The magnetization curves at 300 K and 4.2 K after irradiation and the thermal cycle at 2 kOe exhibited a similar diamagnetic behaviour to that of the pristine sample with a small and positive magnetic contribution appearing above the previous diamagnetic background. The main outcome of the irradiation seemed to be a paramagnetic contribution but there were additional superparamagnetic and ferromagnetic-like contributions which were also observed.

The SQUID magnetometry results clearly indicated that there was a change in the magnetization of the diamond sample after irradiation. The signal appeared to be weak from the SQUID results but that was a result of working on a small area that was irradiated and therefore measuring the magnetic signal coming from the sample resulted in small changes being observed.

To better understand the source of the additional superparamagnetic and ferromagnetic-like contributions, we further went on to perform Raman

and MFM measurements over the irradiated area. From the Raman spectra obtained, an apparent blueshit was observed in the main diamond peak that was relative to 1332 cm^{-1}, this peak should not be observed since there is no reason to observe any structural changes in pristine diamond. As for the irradiated region that was not graphitized, we observed a little disorder within the structure of diamond as expected on an area that was heavily irradiated by protons. The damage was tens of microns into the sample. The third region that was observed is the graphitized region where we observed the G-peak at around 1600 cm^{-1} of the damaged diamond that is beyond the graphitization limit.

What we observed over the irradiated region is a mixture of the $sp3$ and $sp2$ orbitals that are related to the peak at 1330 cm^{-1} of diamond and the 1580 cm^{-1} peak related to the G-band of graphite. We also observed a lot of background noise and certain peaks related to a plethora of other defects in the diamond as a result of the irradiation. The $sp2$ orbitals corresponded to the micro-polycrystalline graphite that is often seen in irradiated diamond. It has been previously observed that the defects have a tendency of clustering into graphitic islands and swell after high dose implantations. The Raman analyses indicated that there was no thin film of dirt above or on the irradiated area, therefore any magnetic signal observed from MFM measurements and from SQUID analysis can and should be attributed to the ion induced modification of the diamond.

Low temperature MFM measurements were performed over the D1 stripe that was studied in the Raman measurements. A magnetic signal was seen in the MFM image with a negative contrast, this was observed by the darker regions relative to the pure diamond corresponding to the graphitic/graphitized region in the topography image. The negative contrast was not completely clear in the MFM image but it can be observed that there is a change in contrast between the irradiated and un-irradiated region. From the SQUID analyses, Raman measurements and MFM analysis, we can safely conclude that the irradiation resulted in the mixture of $sp2$ and $sp3$ orbitals that graphitized the irradiated surface. As it was concluded from the Raman analyses, any magnetic signal measured over the graphitized irradiated region is attributed to the ion induced modification of the diamond structure.

Further MFM analyses are still ongoing to study the irradiated regions to confirm that the graphitized region is the source of the magnetic signal. Confirmation of this will lead to the possibility of inducing ferromagnetism in diamond through high fluence proton irradiation that could lead to various applications within the microelectronics, spintronics, quantum cryptography, ultraviolet light-emitting diodes and optics, and high-power microwave electronics fields [62].

Bibliography

[1] C.H. Olk J. Heremans and D.T. Morelli. Magnetic susceptibility of carbon structures. *Phys. Rev. B*, 49(20):123 – 125, 1994.

[2] H.O. Pierson. Handbook of Carbon, Graphite, Daimond and Fullerenes, Daimond and Fullerenes. *Mill Road, Park Ridge, New Jersey 07656: Noyes Publications*, pages 244 – 277, 1993.

[3] K. Miyoshi. Structures and Mechanical Properties of Natural and Synthetic Diamonds. *NASA/TM*, pages Cleveland, Ohio, 1998.

[4] R. Wentorf F. Bundy, H.M. Strong and Jr. Chemistry and Physcics of Carbon. *Marcel Dekker Inc.*, 10:P.L. Walker, Jr and P A. Throwerr, Eds., 1973.

[5] T. L. Makarova. Magnetic Properties of Carbon Structures. *Semiconductors*, 38:615–638, 2003.

[6] S. Bundell. Magnetism in Condensed Matter. *New York*.

[7] M. McElfresh. Fundamentals of Magnetism and Magnetic measurements featuring Qunatum Design's Magnetic Property Measurement System. *Quantum Design*.

[8] G Design. *[Online]*, mmrc.caltech.edu/MPMS/Manuals/QD[Accessed 24 August 2017].

[9] A. Gottdang. A new range of high-current Tandetron accelerator systems with terminal voltages of 1-6 MV. *Nuclear Instruments and Methods in Physics Research B*, 219-220.

[10] I.R. Lewis and H Edwards. Handbook of Raman Spectroscopy. *CRC Press*, pages 1 – 4, 2001.

[11] W. Heisenberg. Zur Theorie des Ferromagnetismus. *Z. Phys.*, 49:615–636, 1928.

[12] N. Mutaga. Possible ferromagnetic states of some hypothetical hydrocarbons. *Theoret. Chem. Acta (Berl.)*, 10:372–376, 1968.

[13] M. Fukuda S. Mizogami, M. Mizutani and K. Kwabata. Abnormal ferromagnetic behavior for pyrolytic carbon under low temperature growth by CVD method. *Synth. Met.*, 41 - 43:3271 – 3274, 1991.

[14] L. P. Le; A. Keren; G. M. Luke; W. D. Wu; Y. J. Uemura; M. Tamura; M. Ishikawa; and M. Kinoshita. Searching for spontaneous magnetic order in an organic ferromagnet. μSR studies of β-phase p-NPNN. *Chem. Phys. Lett.*, 206:405 – 408, 1993.

[15] A. Koch F. Wudi K. Holczer S. Donovan G. Gruner P. Allemand, K. C. Khemani and J. D. Thompson. Organic Molecular Soft Ferromagnetism in a Fullerene C_{60}. *Science*, 253:301 – 303, 1991.

[16] Y. Murakami and H. Suematsu. Magnetism in C_{60} induced by photo-assisted oxidation. *Pure and Applied Chem.*, 68:463 – 467, 1996.

[17] H. Ueda K. Murata, H. Ushijima and K. Kawaguchi. A stable carbon-based organic magnet. *J. Chem. Sco. Chem. Commun.*, 7:567 – 569, 1992.

[18] R. Hohne A. Setzer K. H. Han P. Esquinazi, D. Spemann and T. Butz. Induced Magnetic Ordering by Proton Irradiation in Graphite. *Phys. Rev. Lett.*, 91(21), 2003.

[19] A. A. Ovchinnikov and V.N Spector. Organic ferromagnets. New results. *Synthetic Metals*, 27:615–624, 1988.

[20] K. Kusakabe and M. Maruyama. Magnetic nanographite. *Phys. Rev. B*, 67(092406), 2003.

[21] H. Ajiki K. Wakabayashi, M. Fujita and M. Sigrist. Electronic and magnetic properties of nanographite ribbons. *Phys. Rev. B*, 59(8271), 1999.

[22] M.A. Ramos A. Climent-Font A. Zucchiatti A. Munoz-Martin S. Shrivastava T.N. Makgato, E. Sideras-Haddad and R. Erasmus. Magnetic properties of point defects in proton irradiated diamond. *Journal of Magnetism and Magnetic Materials*, 413:76 – 80, 2016.

[23] T.N. Makgato M. Garcia-Hernandez A. Climent-Font A. Zucchiatti N. Daya, E. Sideras-Haddad and M.A. Ramos. Investigation of the magnetic properties of proton irradiated type Ib HPHT diamond. *Diamond and Related Materials*, 64:197 – 201, 2016.

[24] A. Yanase K. Kenmochi, K. Sato and H. Katayama-Yoshida. Materials Design of Ferromagnetic Diamond. *Japanese Journal of Applied Physics*, 44(2).

[25] Q. Wahab M. Willander, M. Friesel and B. Straumal. Silicon carbide and diamond for high temperature. *Journal of Material Science*, 17:1 – 25, 2006.

[26] P. Stamenov. Magnetic susceptibility of carbonexperiment and theory. *Journal of Magnetism and Magnetic Materials*, pages 290 – 291, 2005.

[27] GCSEScience. *[Online]*, gcsescience.com, [Accessed 09 November 2015].

[28] R. Kalish M.S. Dresselhaus. Properties of Diamond, in Ion implantation in Diamond, Graphite and Related Materials. *Springer-Verlag*, Berlin:21 – 25, 1992.

[29] G. Chimowa. Synthesis and Characterization of Nano-crystalline Diamond Films. *University of the Witwatersrand*, 2011.

[30] D.M. Adams. Inorganic Solids. *John Wiley and Sons*, page New York, 1981.

[31] M. Scharff J. Lindhard and H. Schiott. *Mat. Fys. Medd. Dan. Vid. SelskSpringer-Verlag*, 33(14), 1963.

[32] M.T. Robinson and O. Oen. The Channeling of Energetic Atoms in Crystal Lattices. *Applied Physics Letters*, 2(2):30 – 32, 1963.

[33] NTCU OWC. [Online]. *Available http://ocw.nctu.edu.tw/upload/classbfs1209042706186759.pdf*, [Accessed 06 November 2015].

[34] C. Kittel. Diamagnetism and Paramagnetism, in Introuction to Solid State Physics. *John Wley and Sons, Inc*, pages 415 – 440, 1996.

[35] Hyperphysics. Goergia State University - Depaertment of Physics and Astronomy. *[Online]*, Available http://hyperphysics.phy-astr.gsu.edu/hbase/tables/magprop.html, [Accessed 06 November 2015].

[36] V. Heera R. Hohne, P. Esquinazi and H. Weishart. Magnetic properties of ion-implanted diamond. *Diamond and Related Materials*.

[37] M. Benz. Superparamagnetism: Theory and Applications - Discussion of two papers on magnetic nanoparticles. 2012.

[38] A. Chen J. Bowles, M. Jackson and P. Solheid. Interpretation of Low-Temperature Data Part 1: Superparamagnetism and Paramagnetism. *The IRM Quarterly*.

[39] G.C. Papaefthymiou. Nanoparticle magnetism. *Nano Today*.

[40] G. Aviv. SQUIDs - Superconducting Quantum Interference Devices. *Be'er-Sheva Isreal*, 2008.

[41] H. Rogalla. Consequences and Applications: Flux quantazation. *100 years of supercoductivity*, page 58, 2011.

[42] J. Clarke. The SQUID Handbook. *Germany, WILEY-VCH Verlag GmbH and Co*, 2004.

[43] P.W. Anderson. Probable observation of the Josephson tunneling effect. *Phys. Rev. Lett.*, 10.

[44] Supra Design. [Online]. *Available http://www.supraconductivite.fr/en/index.php?p=applications-squid-josephson*, [Accessed 18 November 2015].

[45] A. M. Majcher. Magnetic properties of molecular transition metals compound. Krakow.

[46] American Magnetics. [Online]. *Available http://www.americanmagnetics.com/charactr.php*, American Magnetics Inc, 1968, [Accessed 17 November 2015].

[47] INDIAN INSTITUTE OF SCIENCE. [Online]. *Available http://ipc.iisc.ernet.in/ magsquid/contents.html*, [Accessed 17 November 2015].

[48] V. Kose. Detection Coil Configurations, in Superconducting quantum electronics. *Springer-Verlang*, Berlin Heidelberg.

[49] A.C. Rose-Innes. Introduciton to superconductivity. *Oxford*, Pergamon Press.

[50] D. J. Bland. Condensed Matter Physics. *University of Liverpool, 15 03 2003*, [Online]. Available http://www.cmp.liv.ac.uk/frink/thesis/thesis/node47.html., [Accessed 19 November 2015].

[51] J. A. Echenique. The Centre for Micro Analysis of Materials. *Universidad Autnoma de Madrid*, [Online]. Available https://www.cmam.uam.es/en/facilities/accelerator/94, [Accessed 05 September 2015].

[52] Alexander Wu Chao. Handbook of Accelerator Physics and Engineering. *Singapore*, World Scientific Publishing.

[53] A. Gottdang. The novel HVEE 5 MV Tandetron. *Nuclear Instruments and Methods in Physics Research B*, 190.

[54] R. Allenspach and A. Bischof. Spin-polarized secondary electrons from a scanning tunneling microscope in field emission mode. *Applied Physics Letters*, 54(6):587 – 589, 1989.

[55] S. Russek B. Jeanneret R. Ono J. Moreland, P. Rice and D. Rudman. Scanning tunneling microscopy of the surface morphology of .... *Applied Physics Letters*, 59(23), 1991.

[56] S. Dror. Chapter 12 Magnetic Force Microscopy, in Scanning Force Microscopy with Applications to Electric, Magnetic and Atomic Forces. pages 153 – 180, 1994.

[57] W. Eckstein. Computer Simulation of Ion-Solid Interactions. *Springer Ser. Mater. Sci*, 10, 1991.

[58] J.P. Biersack and L.G. Haggmark. A Monte Carlo computer program for the transport of energetic in amorphous targets. *Nucl. Inst. and Meth*, 174(257), 1980.

[59] J. Ziegker. The Stopping and Range of Ions in Matter. *New York: Pergamon Press*, 1977.

[60] H.A. Szymanski. Raman Spectroscopy, Theory and Practice. *Springer Science and Business Media*, page 1, 2012.

[61] Q. Design. Quantum Design Inc. *[Online]*, https://www.qdusa.com/sitedocs/appNotes/ppms/1096-306.pdf, [Accessed 06 January 2016].

[62] B.D.D. Awschalom and R. Hanson. Diamond age. *Sci. AM.*, 2007.

[63] K. K. Likharev. Superconducting weak links. *Rev. Mod. Phys.*, 51.